Atmospheric
Measurement
Techniques

Algorithms and uncertainties for the determination of multispectral irradiance components and aerosol optical depth from a shipborne rotating shadowband radiometer

Jonas Witthuhn[1], Hartwig Deneke[1], Andreas Macke[1], and Germar Bernhard[2]

[1]Leibniz Institute of Tropospheric Research, Remote Sensing, Leipzig, Germany
[2]Biospherical Instruments Inc., San Diego, CA

Correspondence to: Jonas Witthuhn (jonas.witthuhn@tropos.de)

Abstract. The 19-channel rotating shadowband radiometer GUVis-3511 built by Biospherical Instruments provides automated shipborne measurements of the direct, diffuse and global spectral irradiance components without a requirement for platform stabilization. Several direct sun products, including spectral direct beam transmittance, aerosol optical depth, Ångström exponent and precipitable water, can be derived from these observations. The individual steps of the data analysis are described, and the different sources of uncertainty are discussed. The total uncertainty of the observed direct beam transmittances is estimated to be about 4 % for most channels within a 95 % confidence interval for shipborne operation. The calibration is identified as the dominating contribution to the total uncertainty. A comparison of direct beam transmittance with those obtained from a Cimel sunphotometer at a land site and a manually operated Microtops II sunphotometer on a ship is presented. Measurements deviate by less than 3 and 4 % on land and on ship, respectively, for most channels and in agreement with our previous uncertainty estimate. These numbers demonstrate that the instrument is well suited for shipborne operation, and the applied methods for motion correction work accurately. Based on spectral direct beam transmittance, aerosol optical depth can be retrieved with an uncertainty of 0.02 for all channels within a 95 % confidence interval. The different methods to account for Rayleigh scattering and gas absorption in our scheme and in the Aerosol Robotic Network processing for Cimel sunphotometers lead to minor deviations. Relying on the cross calibration of the 940 nm water vapor channel with the Cimel sunphotometer, the column amount of precipitable water can be estimated with an uncertainty of ±0.034 cm.

1 Introduction

Aerosol and clouds are important components of the earth's climate system. Detailed knowledge of their interactions as well as their radiative properties and effects is crucial to advance our understanding of climate change (Boucher et al., 2013). One specific aspect which requires further research is their interaction with solar radiation through scattering and absorption and the resulting modulation of the shortwave radiation budget.

Focusing on aerosols, the Aerosol Robotic Network (AERONET) provides a relatively dense observational network of aerosol optical depths (AODs) and further properties retrieved from Cimel sunphotometers over land (Holben et al., 1998). The Multi-filter Rotating Shadowband Radiometer (MFRSR) established by the US Department of Energy's Atmospheric Radiation Measurement (ARM) Climate Research Facility is another widely used instrument to measure spectral irradiance components, aerosol and cloud optical properties (Harrison et al., 1994; Hodges and Michalsky, 2011).

Over ocean, however, our knowledge about aerosol properties and climatology is limited due to the low density of observations (Haywood et al., 1999). Compared to the techniques used over land, shipborne observations are also more

challenging due to the continuously moving nature of the platform caused by waves.

To address this point, the Maritime Aerosol Network (MAN) has been established as a subproject of AERONET. It uses handheld Microtops II sunphotometers (referred as Microtops in the following text) and thus relies on the skill of human observers to compensate for the ship movement (Smirnov et al., 2009). Using sunphotometers on stabilized platforms is one alternative, but it requires highly complex hardware, which so far is too expensive for wide spread use. The shadowband radiometer offers a promising alternative to the stabilization or manual tracking of sunphotometers for shipborne operation, if a constantly moving shadowband is used (Reynolds et al., 2001). In addition, it provides direct information about irradiance components and thus aerosol and cloud radiative effects. This type of radiometer observes spectral irradiance with a high sampling frequency, while a shadowband sweeps across the upper hemisphere and causes a well-defined shadow to fall on the sensor during its transit. From this time series, it is possible to identify the measurements when the sun is blocked and to estimate the direct component of the solar radiation even if the platform (e.g., the ship) moves, as long as the orientation of the sensor is known.

The simultaneous measurement of spectral irradiance components with a single radiometer avoids inconsistencies in calibration which are unavoidable if multiple radiometers are used. Also, the calibration uncertainty can be neglected for direct to diffuse irradiance ratio products, because both components are measured with the same sensor. Aerosol size distributions can be obtained from the spectral dependence of the AOD (King et al., 1978). High-frequency sampling combined with a narrow shadowband can offer additional information about the distribution of circum solar radiation and can potentially be exploited to retrieve cloud optical depth and effective radius (Min and Duan, 2005; Bartholomew et al., 2011).

Within the framework of the OCEANET project (Macke, 2009), a shipborne facility was developed for long term investigation of the transfer of energy, particles and chemical compounds between ocean and atmosphere. Since 2009, 12 cruises have been conducted with detailed atmospheric measurements on the German research vessel *Polarstern* during its meridional transfer cruises between the hemispheres, including aerosol observations as part of MAN. To improve and extend observational capabilities, a GUVis-3511 radiometer (referred as GUVis in the following text) was acquired in 2014 from Biospherical Instruments Inc. (BSI), which is equipped with a shadowband accessory termed BioSHADE (Morrow et al., 2010). The shadowband is designed to perform a sweep with constant speed over the radiometer sensor. The irradiance is measured with 15 Hz during one sweep. The radiometer offers 18 narrow spectral channels ranging from 305 to 1640 nm and 1 broadband channel with a sensitive range from 400 to 1000 nm. It in-

Table 1. Centroid wavelengths (λ_C) and bandwidth (full width at half maximum, or FWHM) of GUVis channels.

Channel (nm)	λ_C (nm)	FWHM (nm)
305	297.4	17.0
340	340.4	8.7
380	380.6	9.1
412	412.0	10.5
443	442.6	8.5
510	508.4	9.5
610	610.8	11.3
625	625.5	9.8
665	665.5	9.8
694	693.6	9.2
750	748.2	10.0
765	764.8	10.3
875	877.3	11.7
940	942.2	11.9
1020	1019.5	10.0
1245	1249.1	16.8
1550	1549.5	13.4
1640	1645.4	28.4

cludes channels with a centroid wavelength close to those of the AERONET Cimel and MFRSR instruments, as well as a number of additional wavelength bands. This wide spectral range and the ability to measure on a ship makes this instrument and its data products unique and will enable us to gain further insight into the properties and radiative effects of aerosol over the ocean.

The goals of this paper are threefold. First, we present the GUVis shadowband radiometer (Sect. 2) and the algorithms implemented at the Leibniz Institute of Tropospheric Research (TROPOS) for the data analysis (Sect. 3). This includes the calculation of the spectral irradiance components including a motion correction for operation on ships and the subsequent retrieval of spectral AODs, Ångström coefficients and atmospheric water vapor column from the direct irradiance measurements (direct sun products). Secondly, an uncertainty analysis of these products is given based on theoretical considerations (Sect. 4). Finally, a comparison is presented with a Cimel sunphotometer over land and Microtops observations over sea, to confirm our accuracy estimates and the reliability of the products (Sect. 5). The paper ends with a discussion (Sect. 6), a summary and an outlook in Sect. 7.

2 Instrumentation

The GUVis radiometer (see Fig. 1) is a multichannel filter instrument (Seckmeyer et al., 2010) with 18 narrow spectral channels, ranging from 305 to 1640 nm with a bandwidth of approximately 10 nm, plus 1 unfiltered broadband channel with a spectral response given by its silicon detec-

Figure 1. The radiometer GUVis-3511 (center) with the BioSHADE accessory (right), which drives the shadowband. The BioGPS accessory is shown in the background on the left. The small white dome in the center of the radiometer top is the diffuser, which covers the filtered detectors.

Figure 2. Idealized irradiance time series measured during one shadowband sweep. When the sun is blocked, some part of the diffuse irradiance (black hatched area) is blocked by the shadowband in addition to the direct sun light. This part is estimated by extrapolation of the data from the time series (blue line). The direct and diffuse irradiance is calculated from data obtained during the sweep. Between the sweeps, the global irradiance is observed.

tor (e.g., King and Myers, 1997). Exact values for the bandwidth and the centroid wavelength of each spectral channel are shown in Table 1. Each channel consists of interference and blocking filters (e.g., UG-11 and BG-25 bandpass filters from Schott) that are coupled to a "microradiometer" (Morrow et al., 2010). Each microradiometer includes a photodetector, preamplifier with three-stage gain, 24 bit analogue-to-digital converter, microprocessor and an addressable digital port. Data streams from all microradiometers are combined with measurements from ancillary sensors (e.g., temperature) and transmitted via a USB port to a PC. The design does not require to multiplex analogue signals from multiple photodetectors, resulting in less electronic leakage and better reliability than traditional approaches. The instrument's internal temperature is stabilized to $40 \pm 0.5\,°C$ using a proportional–integral–derivative controller. Silicon photodiodes are used for channels with wavelengths up to 1020 nm, while channels above this wavelength use indium gallium arsenide detectors. Channels were selected from a list of standard wavelengths equipped with hard-coated ion-assisted deposition interference filters, which are known for excellent long-term stability. For the TROPOS instrument, three custom wavelengths were chosen to optimize the information content for atmospheric retrievals and had to be realized using less durable soft-coated interference filters for cost reasons. Specifically, this applies to the channels at 750 nm as absorption-free reference for the 765 nm oxygen A-band channel, the 940 nm channel to measure the atmospheric water vapor column (Halthore et al., 1997) and the 1550 nm channel for cloud microphysics retrievals (Brückner et al., 2014). Data analysis suggests that the transmission of these soft-coated filters has changed significantly during the deployment of the instrument (Sect. 4.1.2).

The filter microradiometer assemblies point at the center of an irradiance collector, which features a composite diffuser made of layers of generic and porous polytetrafluo-

roethylene (PTFE) sheets (Hooker et al., 2012). This design leads to relatively small cosine errors also in the infrared, where the scattering properties of traditional PTFE diffusers are typically degraded. The instrument is also equipped with two orthogonally mounted accelerometers for determining the instrument's inclination (pitch and roll). The two sensors are not designed for use in a dynamically moving environment, such as on ships, and measurement errors will occur when the instrument's orientation is changing rapidly.

The radiometer is equipped with a computer-controlled shadowband accessory, called BioSHADE (Morrow et al., 2010). The band is made of black anodized aluminium, is 2.5 cm wide and has a diameter of 26.7 cm. Due to its geometry, the shadowband occults a solid angle of 15° of the sky from the sensor in zenith position. The width of the BioSHADE shadowband is broader compared to the MFRSR (3.3°; Harrison et al., 1994) and the thin-cloud rotating shadowband radiometer (TCRSR; 2 and 5°; Bartholomew et al., 2011) and it is not feasible to measure the shape of the solar aureole for thin-cloud retrievals (Min and Duan, 2005). The uncertainty arising from the shadowband width on the calculation of the direct horizontal irradiance is discussed in Sects. 3.2 and 6.

The GUVis typically samples at 15 Hz at all times, including when a sweep is performed. For one sweep, the band rotates 180° over the radiometer diffuser at a constant speed such that at least five data points are sampled during the time when all parts of the diffuser are shaded by the band. For measuring global irradiance, the band is stowed below the horizon of the instrument's diffuser after one sweep during the split time to the next sweep. An idealized time series of one shadowband sweep is shown in Fig. 2. The method to derive the irradiance components from this kind of time series is described in Sect. 3.2.

The instrument is also equipped with a GPS receiver, called BioGPS, which determines latitude, longitude and time once per second, and it adds this information to the data
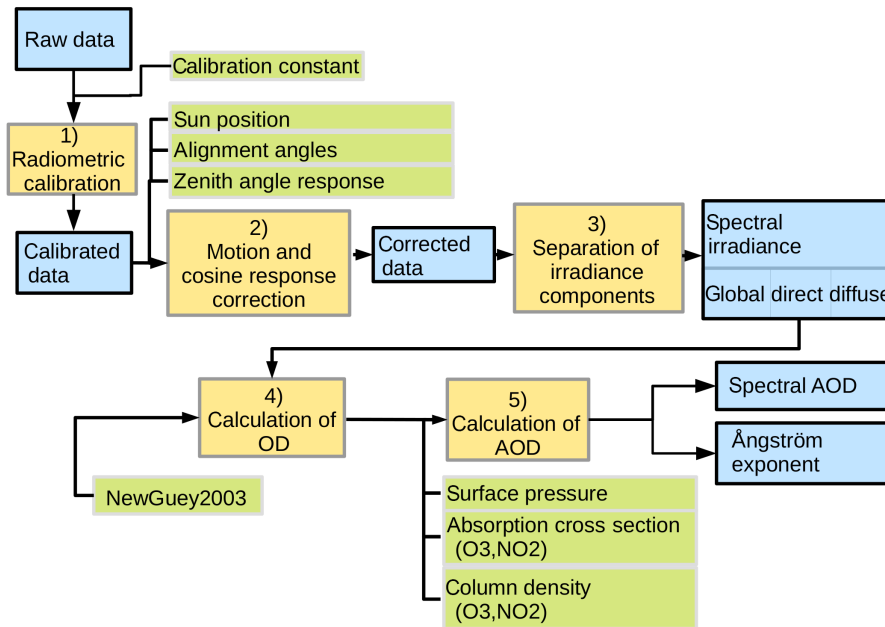
Figure 3. This flowchart outlines the data processing steps for the GUVis observations. Generated data products are shaded in blue, while calculation and processing steps are numbered and shaded in yellow. Supplementary data needed for processing are colored green.

stream. The GUVis is controlled by a data acquisition software running on a Windows laptop, which records the raw sensor signals and the irradiance plus additional status information in ASCII data files.

The instrumental setup is shown in Fig. 1. For operation the GUVis is mounted together with a total sky imager, which is used to identify sky conditions, and as supplementary information for interpreting the irradiance measurements.

3 Method

Raw data are calibrated with calibration coefficients stored in the instrument's internal memory. The calibration has been performed by the manufacturer and includes an absolute calibration, a characterization of the sensor's deviation from the desired cosine response and the determination of the spectral transmission of filters in the laboratory. These calibration data were shipped with the instrument and are used for our calculations and corrections.

For retrieving the direct irradiance and AOD, we have implemented several subsequent algorithms for data processing. These programs provide the separation of the irradiance components as well as the calculation of the spectral AOD. To achieve this, we use the proportionality of the direct horizontal spectral irradiance (DHI, $I(\lambda)$) to the spectral direct beam transmittance $T(\lambda)$ expressed by the Beer–Lambert law (Beer, 1852), which is the fundamental relation also ex-

ploited by sunphotometer observations:

$$I(\lambda) = \frac{I_0(\lambda)\,\mu_0}{R_E^2}\,\exp\left(-m_a\,\tau(\lambda)\right),\tag{1}$$

with $m_a = \mu_0^{-1}$ and

$$T(\lambda) = \frac{I(\lambda)\,R_E^2}{I_0(\lambda)\,\mu_0}.\tag{2}$$

The total spectral optical depth is denoted as $\tau(\lambda)$. For the top-of-atmosphere (TOA) solar irradiance I_0 at an earth–sun distance of 1 astronomical unit, the NewGuey2003 spectrum (Gueymard, 2004) is applied, which is convolved with the spectral response function of the GUVis channels obtained from the manufacturer's instrumental characterization. I_0 is scaled by the inverse square of the actual sun–earth distance (R_E, expressed in astronomical units), which is calculated using equations given by WMO (2010). We assume the air mass factor m_a to be equal to the inverse cosine of the zenith angle μ_0^{-1} here. The deviation from more complex expressions will be small as we are currently not using data with the sun close to the horizon (zenith angle > 70°; see Sect. 3.2).

Data are corrected for ship motion and cosine error of the instrument's irradiance collector. For AOD calculations, the optical depth (τ) for several atmospheric gases and Rayleigh scattering are taken into account. Also, the time series is screened to exclude cloud-contaminated data. The implemented methods are based on the description given previously by Morrow et al. (2010), Bannehr and Schwiesow (1993), Boers et al. (1998), Smirnov et al. (2000) and Alexandrov et al. (2002, 2007, 2008). In the following, the

steps of our data analysis are described. An outline of the processing is given by the flowchart shown in Fig. 3.

3.1 Motion and cosine error correction

Motion and cosine error corrections are applied simultaneously before the actual processing because of their interdependency.

The motion correction compensates for the leveling errors of the instrument due to the ship movement and estimates the deviation from a horizontally aligned irradiance observation. This is crucial because the spectral irradiance is defined either relative to a horizontal reference plane or a plane normal to the solar beam. Due to the ship motion, the alignment of the instrument is changing continuously. This is compensated based on the method described by Boers et al. (1998). A correction factor (C_1), according to Boers et al. (1998), is calculated from the ratio of the cosines of the true solar zenith angle (Θ) and the apparent zenith angle (Θ_A), which is calculated from the sun position and the ship's role, pitch and heading angles. The method from Boers et al. (1998) only corrects the direct irradiance component for the effects of motion and is thus only applicable when the sun is visible. Due to anisotropy in the diffuse radiation field, e.g., due to Rayleigh scattering, the diffuse component of irradiance also changes with the tilt of the sensor. Therefore C_1 can be improved to account for the diffuse irradiance. By adapting the method of Boers et al. (1998) and using radiative transfer calculations, carried out with the libradtran package using the DISORT solver (Mayer and Kylling, 2005), improved correction factors (C_2 and C_3) are calculated. These factors are defined by Boers et al. (1998) as

$$C_1(\Theta, \Theta_A) = \frac{\cos(\Theta)}{\cos(\Theta_A)}, \tag{3}$$

$$C_2(\Theta, \Theta_A, \lambda) = \frac{\cos(\Theta) + B(\lambda)}{\cos(\Theta_A) + B(\lambda)}, \tag{4}$$

$$C_3(\Theta, \Theta_A, \lambda) = \frac{\cos(\Theta) + B(\lambda) \cdot J(\Theta, \lambda)}{\cos(\Theta_A) + B(\lambda) \cdot J(\Theta_A, \lambda)}. \tag{5}$$

where $B = I_{dif}(\lambda)/I_n(\lambda)$ is the ratio of the diffuse ($I_{dif}(\Theta, \lambda)$) to direct normal irradiance at the surface ($I_n(\lambda)$) for $\Theta = 0°$. $J(\Theta) = I_{dif}(\Theta, \lambda)/I_{dif}(\Theta = 0°, \lambda)$ is the diffuse irradiance retrieved by radiative transfer calculations assuming a clear sky with only molecular scattering (e.g., Rayleigh scattering) at the solar zenith angle, normalized to the diffuse irradiance at $\Theta = 0°$. The three correction factors are compared in Fig. 4 for the 305 and the 510 nm channels. For smaller wavelengths B is close to 1 and the diffuse irradiance becomes more dominant, and therefore C_2 of the 305 nm channel deviates strongly from C_1. Because of the stronger Rayleigh scattering, the diffuse irradiance at shorter wavelengths drops faster than the direct irradiance at lower sun elevation. Due to this effect, the deviation between C_1 and C_3 for channels with wavelengths around 305 nm has

the largest values for solar zenith angles between 60 and 70°. The deviation is small and becomes less important for longer wavelengths due to the fact that Rayleigh scattering is almost negligible for wavelengths greater than 800 nm. Overall, except for short wavelengths around 300 nm, the deviation of the correction factor C_1 to C_2 and C_3 increases with decreasing sun elevation. Effects from aerosol are neglected in the radiative transfer calculations and the uncertainty resulting from this omission for the motion correction factor C_3 is investigated in Sect. 4.1.1.

For measurements on the research vessel *Polarstern*, data from the ship's marine inertial navigation system are used for motion correction. This system provides precise measurements of the roll, pitch and heading angles of the ship at high temporal resolution. Because the instrument is not perfectly aligned relative to the ship's navigation system, we also apply a correction to account for this misalignment. This is done using the method of Bannehr and Schwiesow (1993), choosing data from clear days when the ship moves while the sun is either in the front, back or the sides of the ship. In these cases, the tilt correction is dependent on either the roll or the pitch angles alone. For land operation, the instrument's position is static, but this correction is also applied using the instrument's internal accelerometer measurements to correct for slight misalignments of the setup. The internal measurements of pitch and roll angle have been calibrated using a precision level, and offsets relative to the diffuser are stored in the instrument and corrected by the firmware.

When observing an inclined collimated beam from a horizontal plane with an ideal detector, the measured signal changes with the cosine of the incident zenith angle. The cosine error correction removes the deviation of the instrument's response for an inclined collimated incident beam of radiation from the ideal cosine response. The cosine error Δc of the instrument is taken from a lookup table provided by the instrument manufacturer using Θ_A according to the ship motion. This lookup table has been measured by the manufacturer individually for all spectral channels as part of the instrument calibration. The cosine error correction factor C_C is calculated using the method of Seckmeyer and Bernhard (1993):

$$\begin{aligned} C_C(\lambda, \Theta_A) &= \Delta c(\lambda, \Theta_A) R(\lambda, \Theta_A) \\ &\quad + \Delta c_D(\lambda)(1 - R(\lambda, \Theta_A)), \end{aligned} \tag{6}$$

with

$$c_D(\lambda) = \frac{\int_{2\pi} \Delta c(\lambda, \Theta_A) \cos(\Theta_A) d\Omega}{\int_{2\pi} \cos(\Theta_A) d\Omega}, \tag{7}$$

where $R(\lambda, \Theta_A)$ is the ratio of the direct to global horizontal spectral irradiance obtained from precalculated lookup tables for the different channels and Θ_A. $c_D(\lambda)$ is the diffuse cosine error, calculated from Δc, assuming isotropic diffuse irradiance. Please note that the cosine correction has been found
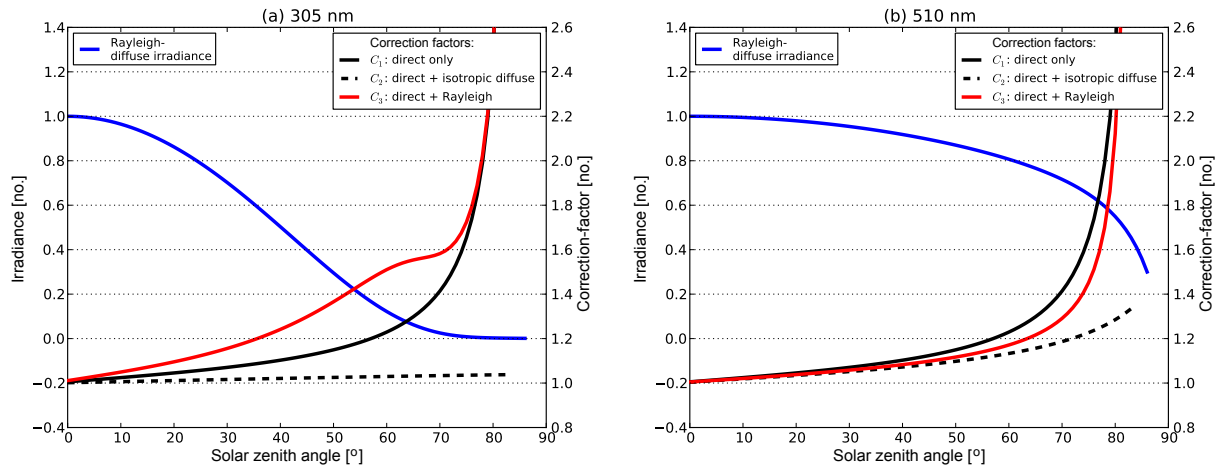
Figure 4. Factors for motion correction measurements of the 305 and 510 nm GUVis channels. The two panels show the calculated diffuse irradiance (blue, left y axis), which is normalized to its maximum. The three correction factors are shown with respect to the right y axis, calculated for an inclination of $6°$ of the ship towards the sun's azimuth angle (e.g., high swell). The direct only (black solid) correction factor refers to C_1 described by Bannehr and Schwiesow (1993). The correction factors C_2 (black dashed) and C_3 (red) are calculated taking direct and diffuse irradiance into account. For C_2, an isotropic diffuse radiance distribution is assumed. C_3 is calculated assuming Rayleigh scattering.

to be virtually independent of wavelength for the range from 305 to 765 nm and of the azimuth angle. Also at this stage, we do not use observations with the sun close to the horizon (solar zenith angle > 70°).

Assuming Rayleigh scattering to calculate the motion correction factors (C_3) is considered to be the most realistic and is used in the present algorithm, based on precalculated lookup tables varying Θ and Θ_A. The cosine error correction factor C_C is calculated from the lookup tables of the instrumental cosine error obtained during calibration. Therefore, the correction of the observed irradiance ($I_m(\lambda)$) to the corrected irradiance ($I_C(\lambda)$) for our processing is defined as

$$I_C(\lambda) = I_m(\lambda) \frac{C_3(\lambda, \Theta, \Theta_A)}{C_C(\lambda, \Theta_A)}. \qquad (8)$$

3.2 Separation of irradiance components

To calculate the irradiance components, the data of each shadowband sweep are analyzed separately. The irradiance is measured with a sampling frequency of 15 Hz during the sweeps. With this temporal resolution, even short-term irradiance fluctuations can be resolved. The global irradiance is observed at the start and end of a shadowband sweep, when the shadowband is outside the field of view of the sensor. The minimum irradiance determined during the sweep corresponds to the time when the diffuser is completely shaded by the shadowband, if the sun is visible. If no clear minimum is identified, the direct irradiance is very small or negligible, and only the global irradiance is determined by the algorithm.

The difference of the global irradiance and the minimum irradiance measured during the sweep represents the direct component of irradiance, together with an additional diffuse part blocked by the shadowband. Figure 2 shows an idealized time series for one sweep (red). The shadowband is designed to block the sun completely for at least five samples of the irradiance. The hatched area represents the blocked diffuse irradiance during the sweep. This occurs because the shadowband blocks a significant part of the sky in addition to the sun. To estimate the amount of blocked diffuse irradiance, 30 data points before and after the transit of the shadow across the diffuser are used to extrapolate the diffuse irradiance for the time when the minimum irradiance is detected (blue line). Values from both extrapolations are averaged. With this information, we can calculate the direct irradiance as the difference between this extrapolated value and the minimum irradiance (Morrow et al., 2010).

It is possible that thick clouds obscure the sun during one sweep. In this case, the data of the sweep will show multiple minima or fluctuations. This behavior is identified by the algorithm and in these cases only the global irradiance is observed. Nevertheless, in situations with thin clouds (e.g., the sun is still visible when obscured by the cloud), the fluctuations are small and processing of the data is still possible. The uncertainty for the retrieved direct irradiance from sweeps with fluctuations in the irradiance data is investigated in Sect. 4.1.3.

With lower sun and increased AOD load, the sweep minimum becomes less pronounced and it is more challenging to identify the shadow of the band on the sensor. Also, the uncertainty of the occulted diffuse irradiance calculated by extrapolation (blue line in Fig. 2) depends on the shape of the solar aureole and varies with aerosol type (Grassl, 1971). The accuracy of extrapolations for different aerosol types and low
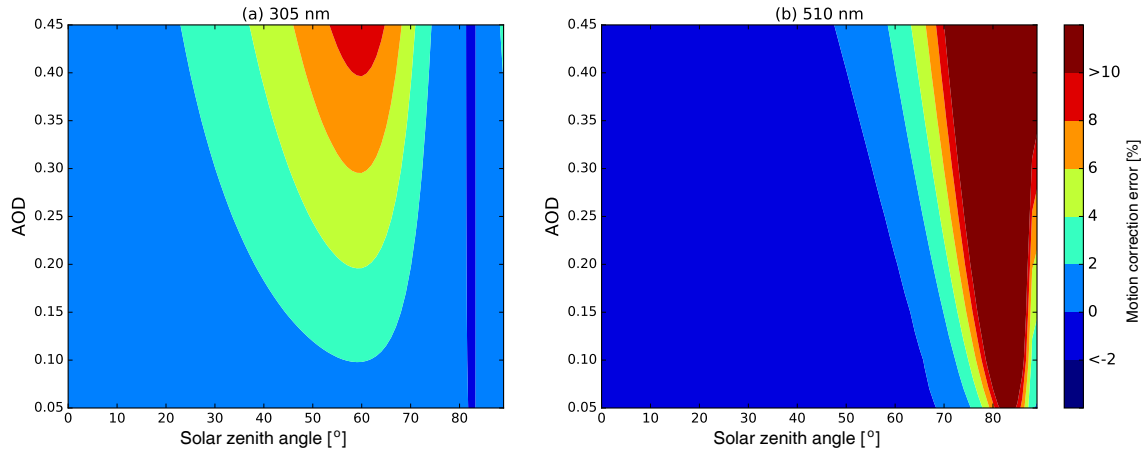
Figure 5. Relative errors in the motion correction for the 305 and 510 nm channel of the GUVis radiometer by not taking aerosols into account. The error is calculated by comparing correction factor $C3$ calculated with no aerosol to correction factors with added aerosol. These correction factors have been calculated like C_3, but using radiative transfer calculations with aerosol type and properties according to Shettle (1990) with AODs of 0.05 to 0.45. The calculations are done for an inclination of 6° of the ship towards the sun's azimuth angle (e.g., high swell).

sun has to be investigated in further work. Preliminary radiative transfer calculations for different aerosol conditions and various solar zenith angles show that the uncertainty from this extrapolation is around 1 % for most conditions with the sun elevated more than 30° above the horizon. This uncertainty may increase when the aerosol has strong forward scattering (eg. desert dust). Nevertheless, an uncertainty of 1 % agrees with the estimation of the "edge-shadow voltage uncertainty" for less variable sweeps observed by Miller et al. (2004). At this stage, we do not use observations with the sun close to the horizon (solar zenith angle > 70°).

3.3 Calculation of τ

From the observed spectral values of DHI, the corresponding total optical depth τ_T of the atmosphere can be calculated from Eq. (1). The total optical depth τ_T is composed of the optical depths for Rayleigh scattering τ_R, trace gas absorption τ_G and aerosol extinction τ_A. In the present algorithm, the gas absorption τ_G takes into account absorption by ozone and NO_2 for all channels, plus H_2O, CO_2 and CH_4 for channels matching the AERONET Cimel sunphotometer (940, 1020 and 1640 nm). The AOD, τ_A, can then be determined by subtracting τ_R (for Rayleigh scattering) and τ_G from τ_T obtained from the measurements.

$$\tau_A(\lambda) = \tau_T(\lambda) - \tau_G(\lambda) - \tau_R(\lambda) \quad (9)$$

In the following, we describe the calculation of τ_R and the individual components of τ_G.

3.3.1 Calculation of τ_R

To calculate τ_R, we have selected the method from Bodhaine et al. (1999), which takes pressure (P), CO_2 concentration

(CO_2) and the gravitational acceleration depending on latitude and altitude into account. A current CO_2 global mean concentration of 400 ppm is assumed and local pressure observations are used. The uncertainty of τ_R is related to the uncertainty of the observed air pressure (see Sect. 4.2.1).

3.3.2 Calculation of τ_{O_3} and τ_{NO_2}

Given the columnar number concentrations n (m^{-2}) of O_3 and NO_2, τ_{O_3} and τ_{NO_2} of these trace gases are calculated as

$$\tau_{O_3} = \sigma_{O_3} n, \quad (10)$$
$$\tau_{NO_2} = \sigma_{NO_2} n. \quad (11)$$

σ denotes the absorption cross section (m^2) of the gases and are taken from Schneider et al. (1987) for NO_2 and (Serdyuchenko et al., 2014) for O_3. Daily values of the columnar number concentration are obtained from the Aura Ozone Monitoring Instrument (AURA-OMI) satellite data (McPeters et al., 2008; Bucsela et al., 2013). The uncertainties of τ_{O_3} and τ_{NO_2} are related to the uncertainty of the observed columnar number concentrations measured by satellites (see Sect. 4.2.2).

3.3.3 Calculation of τ_{CH_4} and τ_{CO_2}

For obtaining the absorption contribution of CH_4 and CO_2 to τ_G, estimates are obtained similarly to the sunphotometer processing by AERONET[1]. The absorption of CO_2 influences observations in both the 1550 and the 1640 nm channel, while the latter is also affected by CH_4 absorption. Based on computations using the standard US 1976 atmospheric

---

[1]http://aeronet.gsfc.nasa.gov/new_web/Documents/version2_table.pdf

model for the 1640 nm channel, τ_{CH_4} was set to 0.0036 and τ_{CO_2} to 0.0089 at a standard atmospheric pressure P_0 of 1013.25 hPa for the 1640 nm channel. The τ_{CO_2} for the 1550 nm channel was set to 0.0007. τ_{CH_4} and τ_{CO_2} are then scaled with the actual air pressure P by $\frac{P}{P_0}$. The uncertainties of τ_{CH_4} and τ_{CO_2} are therefore related to the uncertainty of the measured air pressure (see Sect. 4.2.3).

3.3.4 Calculation of τ_w

The 940 nm channel is used to retrieve the precipitable water using a logarithmic transformation of the measured direct beam transmittance (Smirnov et al., 2004), where coefficients a and b in the following equation are instrument specific constants and are linked to the filter response of the instrument (Pérez-Ramírez et al., 2014). We have chosen to obtain these coefficients from a fit of the shadowband radiometer data to the precipitable water (w) obtained from the Cimel instrument by cross calibration.

The following equation is used to model the atmospheric transmission T_{940} in this channel:

$$T_{940} = T_{940,G} \, T_{940,R} \, T_{940,A} \, T_{940,w}. \tag{12}$$

Here, T_{940} is the measured total atmospheric transmission at 940 nm. The transmissions from gas absorption ($T_{940,G}$) and Rayleigh scattering ($T_{940,R}$) are calculated using the methods described in the previous subsections. The transmission from aerosol ($T_{940,A}$) and water vapor ($T_{940,w}$) is unknown at this stage.

$T_{940,A}$ can be expressed from Eq. (2) as $T_{940,A} = \exp\left(-\mu_0^{-1} \tau_A(940\,\text{nm})\right)$ and estimated using the Ångström exponent calculated from the 440 and 870 nm channels.

To model $T_{940,w}$, the following equation is used:

$$T_{940,w} = \exp\left(-a(w\,m_w)^b\right). \tag{13}$$

$T_{940,w}$ depends on two channel-specific coefficients a and b and the relative air mass factor for water vapor m_w, which is calculated using the method of Kasten (1965).

Equation (12) can be reformulated as a linear equation of the coefficients a and b:

$$\ln\left(\ln\left(\frac{T_{940,A}\,T_{940,R}\,T_{940,G}}{T_{940}}\right)\right) = \ln(a) + b\ln(w\,m_w). \tag{14}$$

From Eq. (14) we have determined values of $a = 0.6131$ and $b = 0.6712$ to best match the precipitable water w retrieved from the Cimel instrument by least-square regression.

With this approach, we avoid the use of spectroscopic data together with the filter response to establish the link between precipitable water and spectral direct beam transmittance. The advantage is that this ensures the consistency with the AERONET observations and allows us to monitor changes in the transmittance of the unstable 940 nm filter using collocated AERONET observations, which are routinely available

at our institute. Due to the fast change of the filter characteristics, it is desirable to carry out these parallel observations frequently, in particular before and after measurement campaigns.

The retrieved precipitable water is related linearly to τ_w at 1640 and 1020 nm to account for the water absorption in these channels (Schmid et al., 1996; Michalsky et al., 1995).

$$\tau_w(1640\,\text{nm}) = 0.0014 \cdot w - 0.0003 \tag{15}$$

$$\tau_w(1020\,\text{nm}) = 0.0023 \cdot w - 0.0002 \tag{16}$$

Due to the reliance of this method on Cimel observations, we cannot estimate τ_w for the 1550 nm channel with this approach. We are planning to derive the relation between τ_w and precipitable water from spectroscopic data for all GUVis channels affected by water vapor absorption in the future.

Comparing the results obtained with our method and the GUVis instrument to the AERONET derived precipitable water, a linear regression shows close agreement, with a slope of 1.001 and a standard deviation of 0.029 cm. Therefore, we conclude that this method is reliable as long as the calibration and filter response of the 940 nm channel remains stable or collocated AERONET measurements are regularly used for cross calibration. The uncertainty for τ_w is estimated from a comparison with the retrievals from the Cimel sunphotometer (see Sect. 4.2.3).

3.4 Cloud mask and quality control

To exclude cloud-contaminated data from the calculation of aerosol properties, we have implemented a cloud mask algorithm as last processing step. Since the temporal resolution of the GUVis instrument is close to that of the Cimel sunphotometer, we utilize the same procedure as described by Smirnov et al. (2000). The time series passes through three processing steps. In the first step, negative AOD values are removed, which may be caused by uncertainties in the correction for Rayleigh or gas absorption during low AOD conditions. The next step identifies triplets of data points with a variability greater than 0.02 in AOD as cloudy, which assumes that the AOD in the total atmospheric column is less variable than this threshold over an interval of 3 min. The last step is a smoothness test, where the time series is compared against a smoothness criterion, and outliers are iteratively removed until the criterion is fulfilled (Smirnov et al., 2000). After this procedure, cloud-contaminated and erroneous data points should be excluded from the subsequent calculation of AOD. Sample validation has been performed by comparing the clear sky identification with sky images from the total sky camera, which is mounted close to the GUVis. For this, we have chosen cases from the Melpitz Column experiment (see Sect. 5 for a brief description) on 16 June 2015, where fast changing and broken cloud situations have been observed. In all cases, no clouds were identified closer than 15° to the sun. For some situations, the cloud cover reaches up to 0.5, while the data are not flagged as cloudy. Therefore, using the

total sky camera in synergy with the GUVis instrument can improve the clear sky identification in future work.

4 Uncertainty estimation

Estimates of the combined uncertainties of the GUVis observations with respect to the observation of spectral horizontal irradiance and the estimation of the AOD are presented in this section.

Uncertainties resulting from the different sources of error are discussed in the following subsections. The combined relative uncertainty of the direct horizontal irradiance (ΔI_T) is calculated from its individual contributions as follows:

$$\Delta I_T = \sqrt{\Delta I_{an}^2 + \Delta I_{mot}^2 + \Delta I_{cal}^2}. \tag{17}$$

The uncertainty of the motion correction (ΔI_{mot}, see Sect. 4.1.1) is taken from a precalculated lookup table, and the calibration uncertainty (ΔI_{cal}, see Sect. 4.1.2) was estimated from the change in responsivities between two consecutive calibrations (the change was smaller than $\pm 2\,\%$ for all stable channels). The uncertainty caused by amplifier noise (ΔI_{an}, see Sect. 4.1.3) is calculated during the processing from the uncertainty of the fit parameters.

Table 3 summarizes the total estimated uncertainty for land and shipborne operation. As mentioned in Sect. 4.1.2, the responsivity of some channels has been found to change significantly and is excluded from the further uncertainty analysis. For the three channels (305, 340 and 380 nm), this issue should be fixed for future measurements due to the modification of the instrument mentioned in Sect. 4.1.2. All other channels show an uncertainty between about 2.5 and 4 % within a 95 % confidence interval for the irradiance measurements on land and ship, respectively.

Due to the logarithmic dependency of τ to I from Eq. (1), the uncertainties of the direct horizontal irradiance ($I_T \Delta I_T$) and the extraterrestrial irradiance ($I_0 \Delta I_0$) are combined and translated to the absolute uncertainty $\Delta \tau$ as follows:

$$\Delta \tau = \mu_0 \sqrt{\left(\frac{\Delta I_T}{I_T}\right)^2 + \left(\frac{\Delta I_0}{I_0}\right)^2}. \tag{18}$$

After all uncertainty components are calculated, the $\Delta \tau_A$ sums up all components:

$$\Delta \tau_A = \sqrt{\Delta \tau^2 + \Delta \tau_R^2 + \Delta \tau_G^2}. \tag{19}$$

The equation includes the contribution of Rayleigh scattering ($\Delta \tau_R$) and gas absorption ($\Delta \tau_G$), which in turn includes the absorption from O_3, NO_2, H_2O, CH_4 and CO_2. The contribution of each component of $\Delta \tau$ is shown in Table 2. Table 3 shows the estimated total uncertainty for the AOD calculations in absolute values for each stable channel. The uncertainty of AOD is less than 0.02 for all channels.

As we investigate the uncertainty of atmospheric transmission ($T \Delta T$) for comparison to sunphotometers later, $T \Delta T$ can be related to the uncertainty of the direct horizontal irradiance ($I \Delta I$) and the absolute uncertainty of the atmospheric optical depth ($\Delta \tau$) of the GUVis as follows from Eq. (1):

$$\Delta I = \frac{dI}{dT} \Delta T = \frac{I_0 \mu_0}{R_E^2} \Delta T, \tag{20}$$

$$\Delta \tau = \frac{d\tau}{dT} \Delta T = -\mu_0 \frac{\Delta T}{T}. \tag{21}$$

4.1 Irradiance uncertainties

In the following, sources of uncertainties are presented which influence the direct irradiance measurement.

4.1.1 Uncertainty of the motion correction

The motion correction factor C_3 described in Sect. 3.1 takes Rayleigh scattering but no aerosol into account (AOD = 0). Calculations with aerosol require knowledge of aerosol optical properties (e.g., size distribution, single scattering albedo, asymmetry parameter, optical depth) which we only can guess at this stage of processing. To avoid time-consuming radiative transfer calculations during the processing, aerosol is neglected completely for the motion correction. To estimate the uncertainty due to this omission, we have calculated correction factors using radiative transfer calculations taking aerosol with properties according to Shettle (1990) into account. The default properties are a rural type aerosol in the boundary layer, background aerosol above 2 km, spring-summer conditions and a visibility of 50 km. For our calculations, the AOD is modified in the range of 0.05 to 0.45 comparing those correction factors to C_3 without aerosol. Figure 5 shows the deviation of C_3 calculated with and without aerosol influence for the 305 and the 510 nm channels for $\Theta_A = \Theta - 6°$ (e.g., high swell). For a smaller difference between Θ and Θ_A (e.g., lower swell), the error will be reduced and turn negative when $\Theta_A > \Theta$.

From these calculations, we estimate the motion correction uncertainty, forcing the AOD to be 0.45, which is a high AOD and rarely observed over ocean. Also, the sky is assumed to be cloud free. The uncertainty is taken from pre calculated lookup tables depending on Θ_A and Θ. At the recent *Polarstern* cruise PS83 the swell conditions were calm for the most time (see Fig. 8), which is defined as misalignment of the ship smaller than 5°. The mean uncertainty contribution of the motion correction to the irradiance measurements from this cruise was about 0.3 % for all channels.

Applying a correction for aerosol and cloudy conditions requires additional information on the ratio of the direct to diffuse irradiance and the anisotropy of the radiation field, which will be the subject of future investigations.

Table 2. Mean absolute uncertainty of retrieved τ from the our scheme, originating from the measured irradiance ($\Delta\tau$), as well as Rayleigh scattering ($\Delta\tau_R$), NO_2 absorption ($\Delta\tau_{NO_2}$), O_3 absorption ($\Delta\tau_{O_3}$) and the combination of H_2O, CH_4 and CO_2 absorption ($\Delta\tau_{rem}$).

Channel (nm)	$\Delta\tau$ (10^{-3})	$\Delta\tau_R$ (10^{-3})	$\Delta\tau_{NO_2}$ (10^{-3})	$\Delta\tau_{O_3}$ (10^{-3})	$\Delta\tau_{rem}$ (10^{-3})
305	64.2	6.2	0.1	182.3	0.0
340	29.7	3.4	0.5	0.4	0.0
380	28.9	2.2	0.7	0.0	0.0
412	19.2	1.6	0.7	0.0	0.0
443	18.8	1.2	0.6	0.0	0.0
510	18.6	0.7	0.3	0.3	0.0
610	18.6	0.3	0.0	1.3	0.0
625	18.6	0.3	0.0	1.1	0.0
665	18.7	0.2	0.0	0.4	0.0
694	18.7	0.2	0.0	0.3	0.0
750	18.0	0.1	0.0	0.1	0.0
765	19.5	0.1	0.0	0.1	0.0
875	18.0	0.1	0.0	0.0	0.0
940	17.6	0.1	0.0	0.0	0.0
1020	18.9	0.0	0.0	0.0	4.8
1245	20.6	0.0	0.0	0.0	0.0
1550	934.9	0.0	0.0	0.0	0.0
1640	19.8	0.0	0.0	0.0	2.9

Table 3. Summary of the main results of our evaluation of the GUVis shadowband radiometer. The relative change in calibration of each channel is shown in column two. Channels with soft-coated filters (750, 940, 1550 nm), and channels affected by a change in transmission of a diffuser insert (305, 340, 380 nm) are excluded from the uncertainty estimate. The mean uncertainty and deviation according to a 95 % confidence interval from our analysis (Sect. 4) are shown for the spectral irradiances for all stable channels for land-based and shipborne observations in columns three and four. The mean uncertainty for the calculation of AOD is shown in absolute values in columns five and six. The linear regression parameters obtained from the comparison of GUVis with Cimel (land-side) and Microtops (shipborne) spectral direct beam transmittance observations are given in the columns 7 to 9 and 10 to 12, respectively.

1 Channel (nm)	2 Calibration deviation (%)	3 ΔI_T land (%)	4 ΔI_T ocean (%)	5 $\Delta\tau_A$ land (10^{-2})	6 $\Delta\tau_A$ ocean (10^{-2})	7 Comparison to Cimel slope (–)	8 σ (–)	9 R (–)	10 Comparison to Microtops slope (–)	11 σ (–)	12 R (–)
305	28.0	–	–	–	–	–	–	–	–	–	–
340	10.9	–	–	–	–	1.019	0.006	0.998	–	–	–
380	2.2	–	–	–	–	1.003	0.008	0.998	1.026	0.029	0.971
412	0.6	2.6	4.4	1.8	2.0	–	–	–	–	–	–
443	2.0	2.5	4.6	1.8	2.0	0.966	0.010	0.997	1.004	0.024	0.967
510	0.6	2.5	3.8	1.8	2.0	1.057	0.013	0.994	1.040	0.028	0.975
610	0.7	2.4	3.7	1.8	2.0	–	–	–	–	–	–
625	0.7	2.5	3.7	1.8	2.0	–	–	–	–	–	–
665	0.6	2.5	3.7	1.8	2.0	1.028	0.015	0.987	1.029	0.026	0.958
694	0.1	2.5	3.8	1.8	2.0	–	–	–	–	–	–
750	18.4	–	–	–	–	–	–	–	–	–	–
765	1.4	2.8	4.0	1.7	1.9	–	–	–	–	–	–
875	1.6	2.5	4.1	1.7	1.9	1.014	0.019	0.961	0.987	0.026	0.974
940	9.2	–	–	–	–	–	–	–	–	–	–
1020	1.2	2.5	4.1	1.9	2.1	1.002	0.015	0.965	–	–	–
1245	0.4	2.8	5.0	1.8	2.0	–	–	–	–	–	–
1550	40.4	–	–	–	–	–	–	–	–	–	–
1640	0.7	2.6	4.2	1.8	2.0	1.013	0.018	0.922	–	–	–

4.1.2 Uncertainty of the calibration and extraterrestrial spectrum

The instrument was calibrated by the manufacturer at the time it was built. It was recalibrated after two years to verify the stability of the instrument. For these calibrations, NIST-traceable 1000 Watt FEL standard lamps have been used. Table 3 shows the deviation of the calibration constants between both calibrations. Most channels show a drift of less than 2 %, which is within the expected range for the temporal drift of such an instrument and agrees with the findings of Schmid and Wehrli (1995) for laboratory calibrations. Additionally, a Langley calibration was performed on clear days at sea level in San Diego after the recalibration to verify the calibration from the laboratory. Solar measurements for Langley calibrations from sea level causes uncertainties due to fast changing conditions in the boundary layer, also the extraterrestrial spectrum is not known to be better than 3.5 % for wavelengths below 400 nm and 0.8 % above (Gueymard, 2004). For channels with hard-coated filters and wavelengths of up to 875 nm, differences between lamp-based and Langley calibrations differed between 0 and 5 %. For channels with wavelengths between 1020 and 1640 nm the difference was 5 to 6 %. Considering that the Langley calibration was performed at sea level under far from ideal conditions, the agreement can be considered good.

A Langley calibration on a high-altitude site for this instrument is desirable and will be done in future. This will decrease the calibration uncertainties to about 1 % (Schmid and Wehrli, 1995). The drift of the spectral filters will be investigated with ongoing laboratory calibrations in the future.

The channels at 305, 340 and, to a lesser extent, at 380 nm show large drifts. These have been attributed to a change in the transmission of a special insert below the instrument's main Teflon diffuser, which is necessary to get an adequate cosine response at wavelengths larger than about 800 nm. BSI has addressed this problem by replacing this insert with a new material in our GUVis instrument. Hence, the stability of these channels should have significantly improved, which nevertheless needs to be verified by future calibrations.

The channels at 750, 940 and 1550 nm also show large deviations. They correspond to the custom channels chosen by TROPOS as mentioned in Sect. 2. These channels use soft-coated interference filters for cost reasons, which have a known lower temporal stability than hard-coated ones, as is confirmed by these findings. In future, the filters could be replaced by hard-coated filters to increase the stability of these channels. At this stage, no replacement of filters is planned for our instruments, and a small calibration uncertainty can only be achieved by frequent calibrations. For the 940 nm channel, this can be realized by cross calibration with AERONET observations in the field, as outlined in Sect. 3.3.

The optical depth calculated from Eq. (1) can only be as certain as the TOA irradiance I_0 is known. In our processing the extraterrestrial spectrum "NewGuey2003" (Guey-

mard, 2004) is used. The uncertainty estimate from Gueymard (2004) range from 3.5 % in the 280–400 nm band to 0.8 % in the 700–1000 nm band. The uncertainty related to each channel of the GUVis is propagated through our processing causing a mean uncertainty of AOD of 0.008 for the 510 nm channel. Absolute mean values for this uncertainty for all channels are presented in Table 2.

4.1.3 Uncertainty caused by amplifier noise

Noise in the electrical amplifiers of the radiometer directly affects the accuracy of the radiation measurements. We have attempted here to estimate the amplitude for each channel, using measurements obtained during the absolute calibration in the laboratory. The amplitude is assumed to be constant for different levels of incident radiation. High-frequency fluctuations in the direct beam transmittance during observations will introduce a similar uncertainty during our processing. Both effects are combined in the following uncertainty analysis.

The uncertainty due to amplifier noise is strongly reduced by averaging, which is in fact done several times by our method for separating the different irradiance components. The global irradiance is measured and averaged for 20 s (300 samples) between two sweeps, resulting in negligible uncertainty. The direct irradiance is, however, estimated using a smaller number of measurement values. First, a mean irradiance is calculated while the diffuser is completely shaded from direct sun from at least five samples for clear sky, low AOD and high sun conditions and more than 10 samples for lower sun, which again reduces the influence of noise. Secondly, the shading of diffuse irradiance is estimated from the sweep data by linear extrapolation using 30 observations before and after the transit of the shadow across the diffuser. The uncertainties of the fit parameters are also calculated, which allow us to determine the uncertainty of the extrapolated values, and are attributed here to the influence of noise. Please note that deviations from the underlying assumption of the linear model could also arise for other reasons, such as variations of the forward scattering peak, e.g., expected for large particles such as dust or ice crystals.

The uncertainty for the DHI during the Melpitz Column experiment (see Sect. 5 for a brief description) does not exceed 0.6 % within a 95 % confidence interval. Since the diffuse irradiance is calculated as the difference of the global and the direct irradiance, and the uncertainty of the global irradiance due to measurement noise is negligible, its uncertainty is set to be equal to that for the direct irradiance.

4.2 AOD uncertainties

In this section, uncertainties of the AOD retrieval are calculated according to Eq. (19).

4.2.1 Uncertainty of τ_R

Since the calculation τ_R is directly proportional to the pressure, the absolute uncertainty $\Delta \tau_R$ is given as

$$\Delta \tau_R = \tau_R \frac{\Delta P}{P}. \tag{22}$$

ΔP is defined by the manufacturer of the weather station Lufft as $\pm 5\,\text{hPa} \approx 0.5\,\%$.

This method assumes a current CO_2 concentration of about 400 ppm, which can vary over time. However, the deviation of τ_R for varying CO_2 concentration of up to 40 ppm difference is only about 0.003 % and therefore negligible.

Absolute mean values for this uncertainty are presented in Table 2.

4.2.2 Uncertainty of τ_{O_3} and τ_{NO_2}

Because of the spectral dependence of absorption, trace gases introduce a wavelength-dependent uncertainty in the calculation of AOD. This uncertainty is mainly determined by the uncertainty of the trace gas column density, which is obtained here from satellite retrievals by the AURA-OMI instrument. The uncertainty of the column density of O_3 is set to 3 % and for NO_2 column density to 20 %, as specified in the OMI algorithm theoretical basis documents (Bhartia, 2002; Chance, 2002) and confirmed by evaluations (McPeters et al., 2008; Bucsela et al., 2013). These uncertainties are directly translated into an uncertainty of τ_G, with different importance for different channels due to the wavelength dependence of both aerosol properties and gas absorption. Absolute mean values for this uncertainties are presented in Table 2.

4.2.3 Uncertainties of remaining gas absorption

The precipitable water is calculated using the 940 nm channel measurements in Eq. (14). From the linear regression of precipitable water derived from both the Cimel and GUVis we have found the standard deviation σ_w to be 0.029 cm. From the AERONET sample data uncertainty estimate (Holben et al., 1998) we calculate the standard deviation as $\sigma_C = 0.017$ cm. From these values we estimate the combined uncertainty of precipitable water Δw observed with the GUVis as

$$\Delta w = \sqrt{\sigma_w^2 + \sigma_C^2} = 0.034\,\text{cm}. \tag{23}$$

Using this equation, we calculate the uncertainty $\Delta \tau_w$ for the 1020 and 1640 nm channel from Eqs. (15) and (16) as $\Delta \tau_w(1020\,\text{nm}) = 7.82 \times 10^{-5}$ and $\Delta \tau_w(1640\,\text{nm}) = 4.76 \times 10^{-5}$.

τ_{CO_2} and τ_{CH_4} are scaled to the ambient pressure and applied only to the 1640 nm channel. Therefore, the uncertainties $\Delta \tau_{CO_2}$ and $\Delta \tau_{CH_4}$ can be calculated from the uncertainty of the pressure measurements, which are assumed to have a value of $\Delta P = 5$ hPa.

This leads to errors of $\Delta \tau_{CO_2}(1640\,\text{nm}) = 4.361 \times 10^{-5}$ and $\Delta \tau_{CH_4}(1640\,\text{nm}) = 1.764 \times 10^{-5}$, respectively.

The uncertainty ($\Delta \tau_{rem}$) for the absorption of CO_2, CH_4 and precipitable water is combined as follows for the 1640 nm channel:

$$\Delta \tau_{rem} = \sqrt{(\Delta \tau_{CO_2})^2 + (\Delta \tau_{CH_4})^2 + (\Delta \tau_w)^2}. \tag{24}$$

Absolute mean values for this combined uncertainty are presented in Table 2.

5 Evaluation

The Melpitz Column experiment took place between May and July 2015 in a rural area at the TROPOS measurement site Melpitz near Leipzig in Germany. During this time a variety of aerosol and boundary layer measurements were conducted to investigate the aerosol distribution in the whole tropospheric column. To verify the reliability of the GUVis shadowband radiometer, it has been deployed during the Melpitz Column field experiment on land together with a Cimel sunphotometer participating in the AERONET network, which allows a direct comparison of the observations and products.

As the main strength of the GUVis is its ability to be operated on ships, measurements during the cruise PS83 with the RV *Polarstern* are also analyzed here and are compared to MAN observations with a Microtops sunphotometer.

5.1 GUVis vs. Cimel observations

To verify our estimate of the uncertainty of the GUVis instrument as discussed in the previous section, we have operated the instrument in close vicinity of an AERONET Cimel sunphotometer during the Melpitz Column campaign. AERONET sunphotometers have a very strict calibration and quality assurance protocol and are thus used as reference observations here. On land, when stabilization is not an issue, sunphotometers are also the preferred method for aerosol characterization due to the fact that the direct normal and not the direct horizontal irradiance is measured. Firstly, this results in a better signal-to-noise ratio particularly at low sun elevations. Secondly, the separation of irradiance components is avoided, which introduces an additional uncertainty in the data analysis of shadowband radiometer measurements. Comparing both instruments is a good benchmark to test the reliability of the shadowband radiometer observations and the derived data products.

A comparison of GUVis and Cimel observed spectral direct beam transmittance (T) and AOD is shown in Fig. 6 for three matching channels of both instruments. This comparison was extended for all matching channels and the corresponding regression parameters for T are listed in Table 3. We have decided to compare the transmittance rather than AOD in Table 3 because this quantity is more directly related
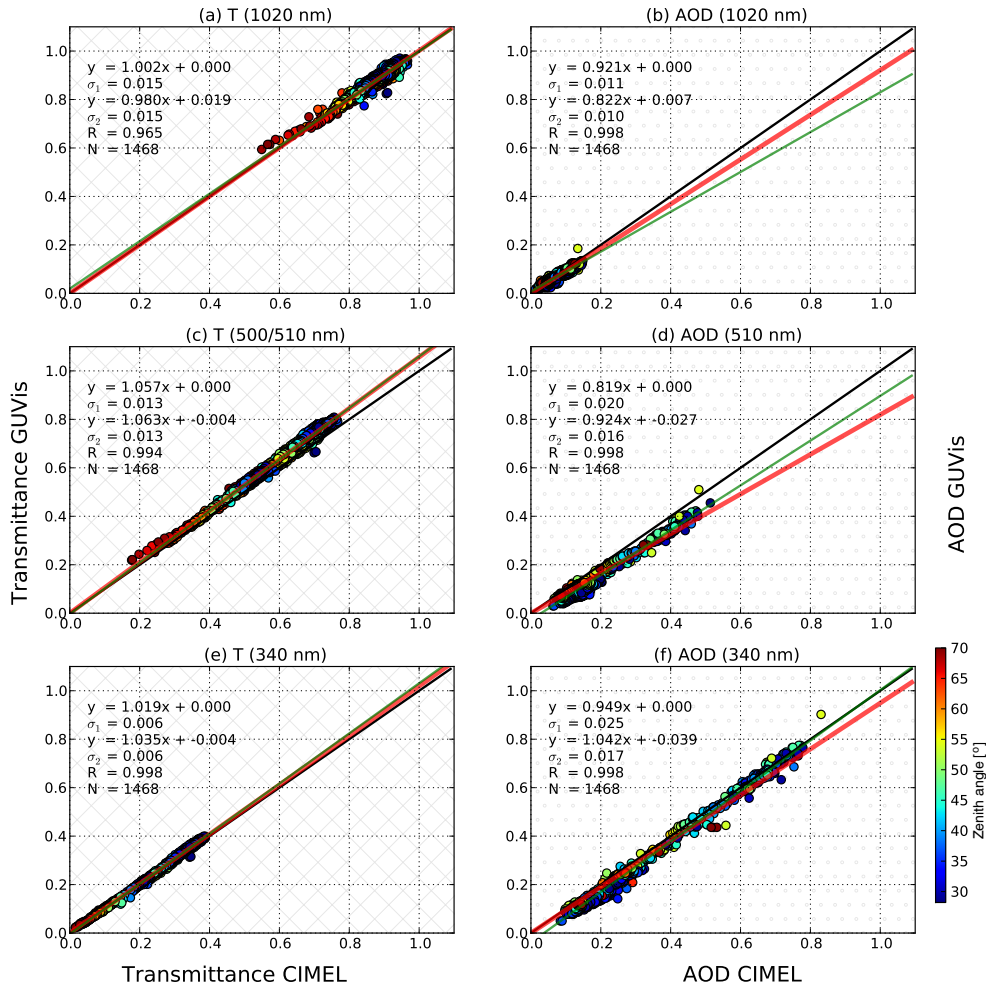
Figure 6. Comparison of the spectral direct beam transmittance (left panels) and spectral AOD (right panels) for three matching channels of the GUVis and Cimel instruments. The parameters of the linear regressions with intercepts forced through zero (first equation) and free intercept (second equation) are denoted in each panel. The deviations from the regression lines are denoted as σ_1 and σ_2. R denotes the correlation coefficient and N the number of available measurement points for comparison. The points are colored with respect to the zenith angle.

to the instrumental measurements. Specifically, the nonlinearity introduced by the Beer–Lambert law and processing uncertainties in Rayleigh scattering and gas absorption are avoided.

T has been calculated from Eq. (2). For GUVis observations, we calculate T directly form the observed DHI. For Cimel observations, the retrieved τ_T as reported by AERONET has been used to calculate the corresponding values of T. The comparison shows a robust linear behavior with increasing deviations for longer wavelengths. The slopes are close to the ideal value of unity for most channels, with a difference below 3 %, except for the 443 and 510 nm channels, which exhibit deviations of about 3.4 and 5.7 %, respectively.

Figure 7 compares τ_R and τ_G obtained from our scheme and the AERONET processing to identify resulting differ-

ences in the retrievals. Here, our retrieval is applied for the central wavelengths given by the Cimel sunphotometer to concentrate on the inherent method differences. The figure shows only small difference of gas absorption optical depths between both algorithms, except for ozone in the 340 nm channel. In general, the differences in τ of both instruments can be explained due to the input data used for calculations. While AERONET uses climatological means for the gas column density of ozone and NO_2, we rely on satellite products from the AURA-OMI satellite instrument. τ_R also shows a minor difference due to deviations of the air pressure measurements. Due to the large wavelength dependence of ozone absorption around 340 nm, the calculated τ_{O_3} strongly depends on the bandwidth of the channel, which is around 10 nm for the 340 nm channel of the GUVis. Due to this, the local minimum in τ_{O_3} at the central wavelength of Cimel
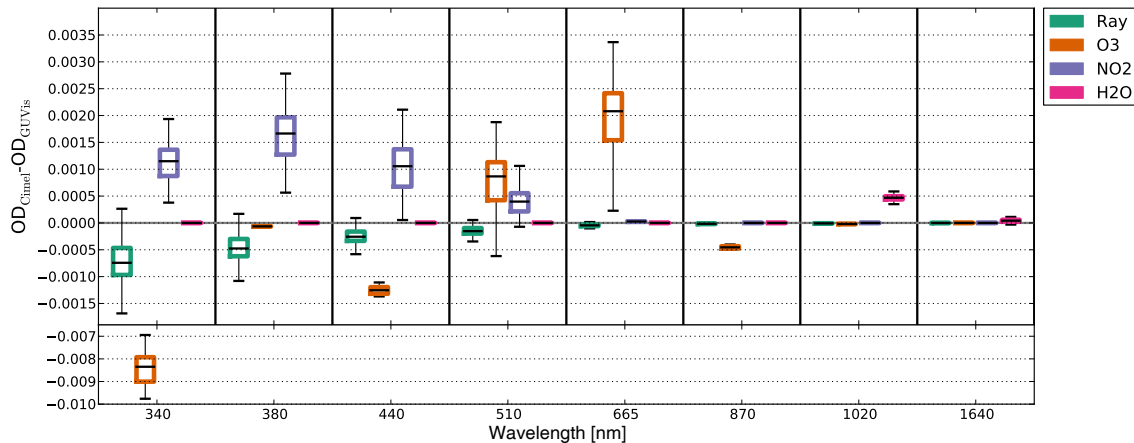
Figure 7. Comparison of the calculated mean τ and its components for matching channels during the Melpitz Column campaign. Shown is the difference of the optical depth components retrieved by AERONET with the Cimel sunphotometer (OD_{Cimel}) and GUVis (OD_{GUVis}) in a box and whisker plot. The median is displayed; the box extends to the 25th percentile and the whiskers towards the 75th percentile of the data. Shown are the optical depth for Rayleigh (Ray), ozone (O_3), nitrogen dioxide (NO_2) and water vapor (H_2O). To highlight the differences in the retrieval scheme, we have adjusted the central wavelengths of the GUVis channels to those of the Cimel instrument. The y axis is split to include the large difference of the 340 nm ozone optical depth.

(341.5 nm) is smoothed out in the GUVis processing. Therefore a large difference of τ_{O_3} is observed for this channel.

Accepting these minor differences, the robust linear behavior shown in Fig. 6 assures us that both instruments provide comparable products, and the deviation from the regression line ΔT can be translated from Eq. (20) into a measurement deviation for both the direct horizontal irradiance (ΔI) and atmospheric optical depth ($\Delta \tau$) of the GUVis, using the observations from the Cimel instrument as reference.

This deviation has been calculated for different situations in the atmosphere (e.g., only marine aerosol, desert dust or continental aerosol). Values for the typical AOD were chosen using the classification scheme from Toledano et al. (2007), and the deviation was estimated using the standard deviation of the direct beam transmittance obtained from the comparison of both instruments. The deviations show a similar magnitude to uncertainties obtained from theoretical arguments in Sect. 4. It also shows that the uncertainty is strongly dependent on the observation conditions, specifically the aerosol loading and sun elevation.

5.2 GUVis vs. Microtops II observations

The German research vessel *Polarstern* is an ice breaker operated by the Alfred Wegener Institute and mainly intended for polar research. In autumn and spring of each year, transit cruises take place across the Atlantic Ocean for transferring the ship into the corresponding polar summer hemisphere. Since 2007, these transit cruises are used to carry out atmospheric measurements within the framework of the OCEANET project (Macke, 2009). During the cruise PS83 in spring 2014, the GUVis shadowband radiometer was operated for the first time as part of OCEANET, with the aim of

providing automated measurements of aerosol optical properties and its radiative effects. The track of this cruise is shown in Fig. 8.

Maritime aerosol consisting of sea salt, sulfate and water was observed throughout the cruise. Continental influences were insignificant in the Southern Hemisphere but became more prominent in the Northern Hemisphere. Mineral dust aerosol as well as biomass burning aerosol was observed while passing along the African coast west of the Saharan desert from 17 until 27 March 2014.

The shadowband radiometer was installed on the navigation deck of the ship as far away as possible from the ship's superstructures to minimize shading effects. Only the mast and chimney as well as the smoke plume of the ship were able to shade the sensor under certain geometries and wind conditions.

Sunphotometer observations with Microtops instruments were also taken during the cruise PS83 as a contribution to the MAN by scientists from the Max Plank Institute of Meteorology (Smirnov et al., 2009). These measurements were carried out manually every 10 to 15 min during clear sky conditions and include five spectral channels ranging from 380 to 870 nm. The handheld photometer is manually pointed towards the sun, taking a sequence of 10 measurements. Before each measurement, the sky condition is checked by eye to be cloud free and to minimize the influence of the ship's smoke plume. Since the Microtops is a handheld instrument, the smoke plume can be avoided by selecting another position on the ship for the measurement, in contrast to the fixed position of the GUVis instrument.

After quality control, the mean of these 10 measurements is stored as a final data set and follow the same processing
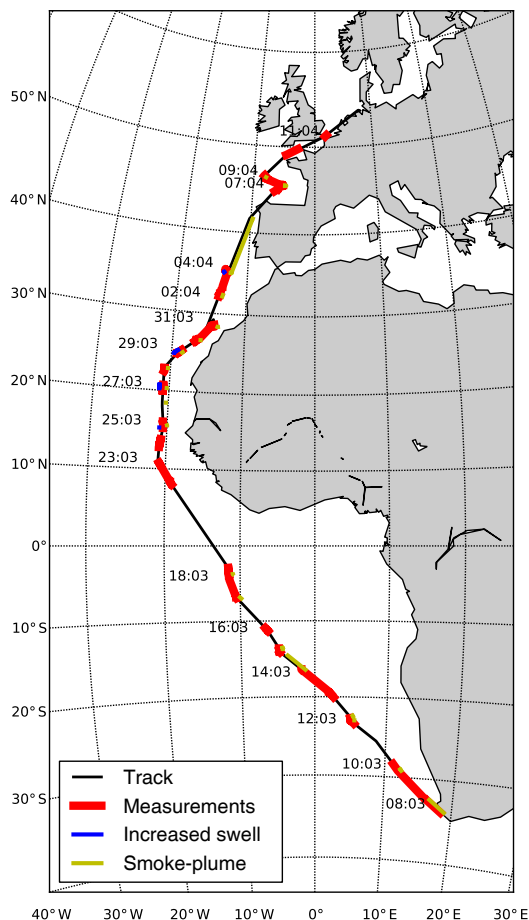
Figure 8. The track for cruise PS83 of the research vessel *Polarstern*. Track points with observations available from both the GUVis and Microtops instruments are marked in red. Additionally, high-swell conditions during the cruise are marked blue, and a possible influence of the ship's smoke plume on GUVis observations is marked in yellow.

protocol as for AERONET Cimel sunphotometers (Smirnov et al., 2002). The data are available from the website of the Goddard Space Flight Center of NASA and are used here as reference for the shadowband radiometer measurements.

The alignment information for the motion correction of the GUVis instrument is taken from the ship's marine inertial navigation system. This system provides precise measurements of the roll, pitch and heading angles with high temporal resolution. Detailed meteorological data are also available from the ship's weather station and can be obtained from the DSHIP database system.

For quality assurance, quality flags were added to the observational data for different conditions. To investigate the influence of the smoke plume of the ship on the measurements, the relative wind speed and direction was used together with the sun position to determine the likelihood of the smoke plume passing between the sun and the shadowband

radiometer sensor. Also, the deviation of the ship from horizontal due to the swell was used for a quality flag. Data with a misalignment of 5° and higher are marked as high swell. Due to larger misalignments of the ship caused by higher swell, the uncertainty of the misalignment correction is expected to increase as described in Sect. 4.1.1.

The comparison shown in Fig. 9, as well as the regression parameters quoted in Table 3, shows an overall agreement of the spectral direct beam transmittance observations from both instruments with a deviation below 4 %, which is in the same range as the comparison to the Cimel sunphotometer. This finding highlights the suitability of the GUVis instrument for shipborne operation. Figure 9 shows a large deviation of the slope calculated form the transmittance comparison and the AOD comparison. The uncertainty $\Delta\tau_A$ is one source which influence the slope of the regression. Also, it should be noted that the optical depth is calculated logarithmically from the transmittance (see Eq. 2), so variations in low transmittance values cause a large impact on the optical depth values and therefore also the regression. For the comparison, only non-flagged data have been considered (e.g., at low swell and no smoke plume over the instrument). In principle, we do expect a strong increase of the uncertainty with increasing swell, but we have been unable to identify this based on the current data, likely due to the limited number of observations with high-swell conditions. In contrast, the influence of the smoke plume can clearly be identified in the comparison, with the smoke flag reliably excluding outliers from the whole data set.

Figure 10 shows the daily mean values of AOD obtained from the Microtops and GUVis measurements during the whole cruise. Also shown is the uncertainty estimate as described in Sect. 4. The GUVis time series has been filtered to only include data points which where recorded within 5 min of a Microtops measurement. The curves obtained from both instruments agree very well. We observed low AOD for the majority of the cruise. An increase of the AOD is evident while passing the Sahara desert and close to the European continent at the end of the cruise. The difference of the observed AOD from both instruments is also shown in Fig. 10. All matching channels agree within a AOD value of 0.05, except the 380 nm channel, which deviates up to 0.1 during high AOD events.

This behavior can also be seen in Fig. 11, where Microtops and GUVis measurements are classified according to different aerosol types following the method of Toledano et al. (2007). Marine aerosol dominates throughout the cruise as expected. However, desert dust can clearly be identified while passing the Sahara desert. At the end of the cruise, the influence on the continental aerosol type increases.

We plan to continue the investigation of the instrumental uncertainty and the observational accuracy with additional observations from ship cruises in the future to better quantify the effects of swell and different aerosol types.
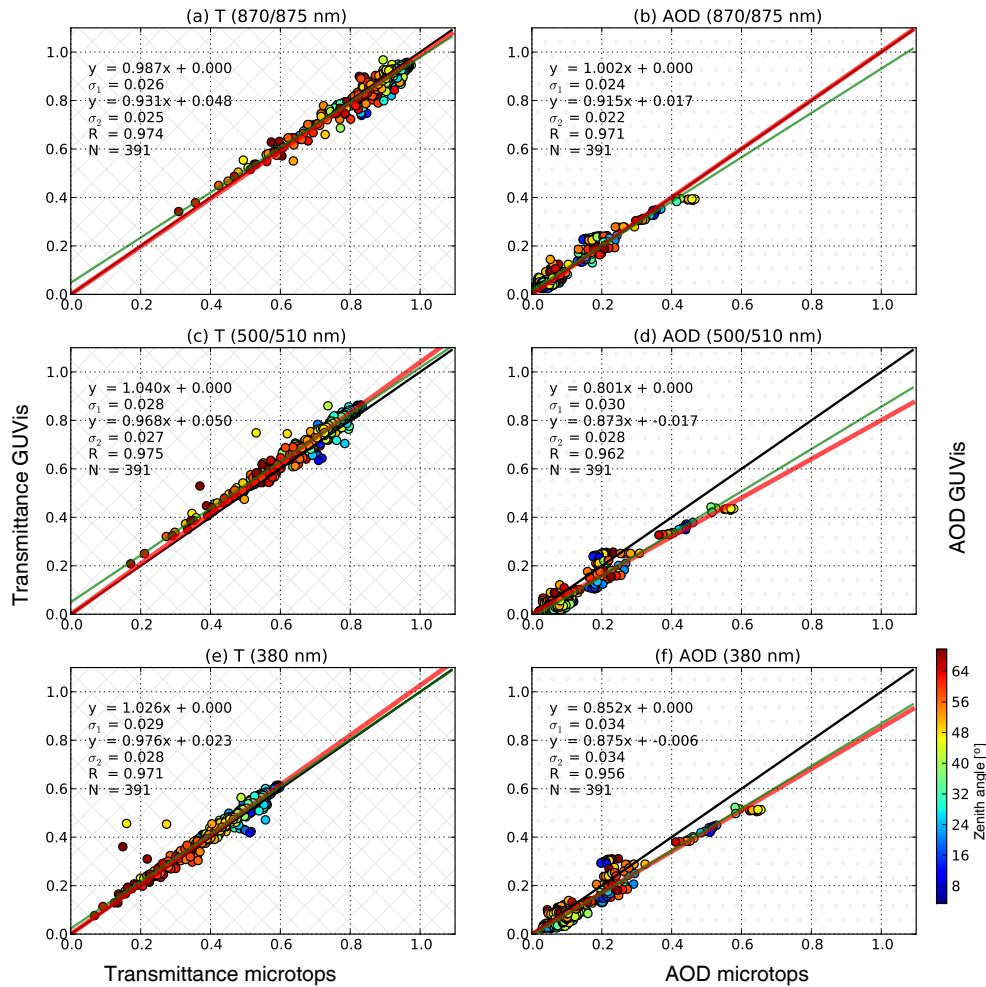
Figure 9. As in Fig. 6 but for the comparison of the GUVis and Microtops instruments during PS83.

5.3 Spectral consistency of AOD observations

To determine whether the observations from each spectral channel of the GUVis are consistent, we assessed the observations in terms of their wavelength dependence. Therefore the deviation of measured AOD is compared to calculated AOD assuming that the wavelength dependence can be modeled by the Ångström exponent plus a curvature term, using a second order polynomial equation according to King and Byrne (1976):

$$\ln\left(\tau_A(\lambda)\right) = a \cdot \ln\left(\frac{\lambda}{\lambda_0}\right)^2 + b \cdot \ln\left(\frac{\lambda}{\lambda_0}\right) + c. \qquad (25)$$

Here, b corresponds to the Ångström exponent. Furthermore, a corresponds to the curvature in $\ln(\tau_A(\lambda))$ versus $\ln\left(\frac{\lambda}{\lambda_0}\right)$ due to the departure of the aerosol size distribution from the Junge power law (Kaufman, 1993) and c to the AOD at a reference wavelength $\lambda_0 = 500\,\text{nm}$. The variables a, b and c have been calculated using a least-squares regression of all

data from the land-side observations during Melpitz Column experiment for GUVis and Cimel and the shipborne observations from PS83 for Microtops.

Figure 12 shows the deviation of AOD and transmittance for all spectral channels of the GUVis, Cimel and Microtops instruments to the calculated value using Eq. (25). We have restricted the calculation of a, b and c to channels with wavelengths of 875 nm and below, because a robust Ångström behavior is only expected for these wavelengths for typical aerosol conditions.

The deviation of AOD from channels below 875 nm from the modeled AOD lies within the estimated uncertainty of AOD of about 0.02 (see Table 3). The deviation of both sunphotometers provides an overall closer match to zero, as well as a lower scatter compared to the GUVis for spectral matching channels. Despite the slightly larger deviations, the spectral dependence suggests that also the non-matching channels, without known issues, work reliably.

The systematic deviations could be minimized by establishing on the cross calibration of matching channels with
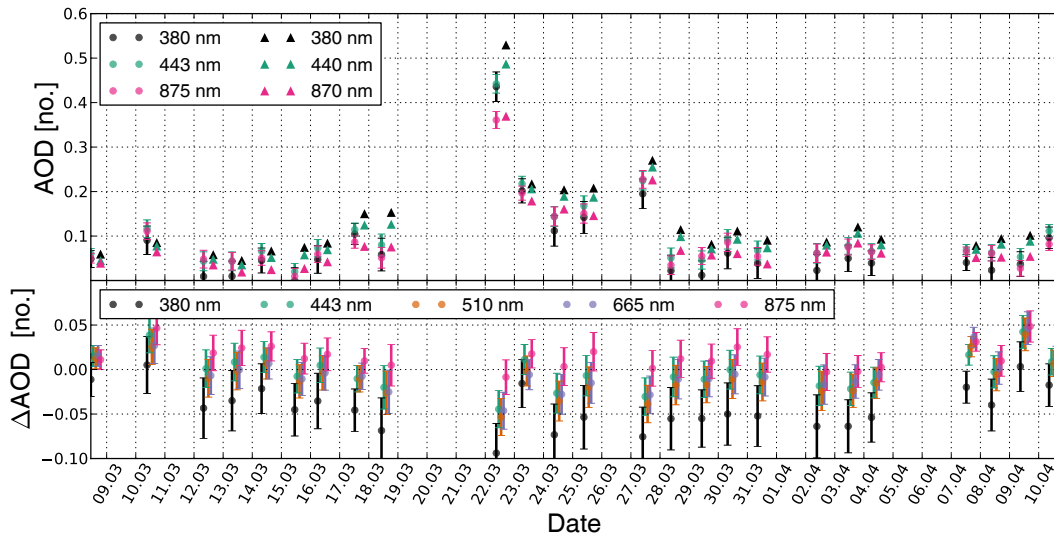
Figure 10. The upper panel shows daily mean retrieved values of AOD for three matching channels from the Microtops (triangle) and GUVis (dot) observations. The lower panel show the differences of all matching channels of the mean observations of AOD from GUVis minus Microtops. Observations of the GUVis within 5 min to the Microtops observations are considered. The error bars of both panels show the estimated uncertainty of the GUVis processing.
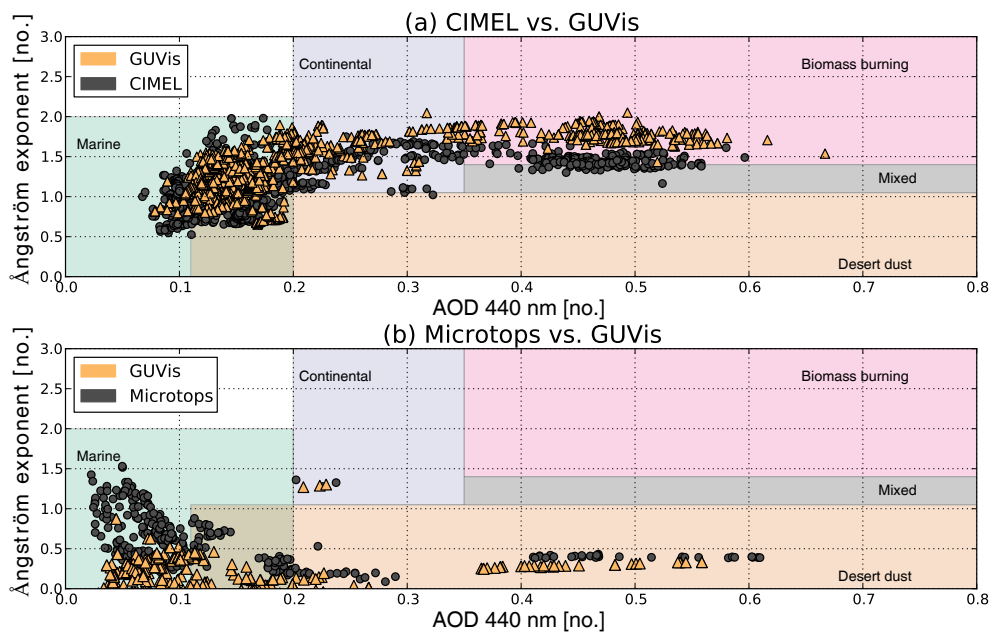
Figure 11. The panels show **(a)** land-side and **(b)** shipborne observations using the Ångström exponent (440–870 nm) and the AOD at 440 nm for aerosol classification as described by Toledano et al. (2007). Sunphotometer observations (grey) are compared to GUVis observations (orange).

the Cimel instrument or a Langley calibration of the GUVis at a high-altitude site, which is planned in the future.

6   Discussion

The theoretical uncertainty estimates of measured irradiance and AOD are shown in Tables 2 and 3. The calibration uncertainty is the dominating contribution to the total measurement uncertainty of the GUVis instrument. Here, we have assumed that the calibration uncertainty is equal to the tem-

poral change between two laboratory calibrations separated by 2 years. This change is found to be less than 2 % for most channels, but it can reach up to 40 % for the channels with soft-coated filters (e.g., the 750, 940, and 1550 nm channels).

From the 940 nm channel, the precipitable water column amount can be inferred with an uncertainty of ± 0.034 cm as shown in Sect. 3.3, if the calibration is well known. Currently, however, the accuracy is limited by the temporal stability of the soft-coated filter used for this channel. While the exchange of the filter with a hard-coated one would be the best solution, frequent intercalibration based on parallel observations with an AERONET Cimel sunphotometer and the methods presented here can also ensure a high level of accuracy.

The channels below 380 nm were also found to have an abnormally high temporal drift. This issue has been attributed to a change in transmission of an insert below the diffuser of the instrument, which has been replaced by the manufacturer with a new material to overcome this issue.

Measurements on land have a smaller uncertainty of the measured irradiance than shipborne observations.

The uncertainty on land is estimated to be 2.5 % within a 95 % confidence interval for the stable channels. This magnitude is confirmed by our comparison with observations from a Cimel sunphotometer during the Melpitz Column campaign (see Sect. 5.1). As the measurement principle of a sunphotometer is more direct than that of the shadowband method of the GUVis instrument, higher accuracy is expected, which is indeed confirmed by our results in Sect. 5.1. Nevertheless, the agreement of matching channels for both instruments is generally within 3 %, corresponding to a standard deviation below 0.02 in direct beam transmittance, illustrating that the GUVis shadowband radiometer can compete with sunphotometer measurements. Some questions remain open, however, for the uncertainty of the 443 and the 510 nm channels, which show comparatively large deviations of 3.4 and 5.7 %, respectively. This uncertainty may result from the fact that the GUVis is calibrated using lamp calibrations and not with the Langley technique which is used to calibrate Cimel sunphotometers.

A slight misalignment of 2 ° during setup on land results in an tilt correction uncertainty of about 0.35 % for observations during the Melpitz Column campaign. This emphasizes that a careful alignment of the instrument is essential to minimize this uncertainty. The amplifier noise cause an uncertainty of about 0.56 %.

If differences in the wavelengths of channels are corrected for, only minor deviations in the AOD retrievals based on the AERONET algorithms and our analysis have been found. These deviations result from the different methods of calculating the ozone and NO_2 absorption. Nevertheless, for wavelength regions with high variability of ozone or NO_2 absorption, the convolution with the channel response function for the calculation of τ_G leads to high deviations when comparing channels with different bandwidths, as stated in Sect. 5.1.

The GUVis is well suited for shipborne observation. Measurements on the ship are, however, additionally influenced by the swell and are expected to exhibit a higher uncertainty than those on land due additional uncertainties introduced by the extrapolation and motion correction steps. Our estimate of the uncertainty for shipborne measurements of the direct beam transmittance is about 4 % within a 95 % confidence interval, which is in agreement with the comparison to Microtops observations during the *Polarstern* cruise in spring 2014 (see Sect. 5.2). Here, deviations up to 4 % have been found for matching channels, as well as standard deviation up to 0.028, which is slightly higher than that found in the comparison with Cimel observations. It has to be noted, however, that we also expect the Microtops sunphotometer observations to be less accurate than those of the Cimel instrument due to manual pointing of the instrument on a ship.

At this stage we were not able to reliably determine the influence of the swell on the observational accuracy. This is mainly due to the limited amount of data available so far, in particular with higher swell due to the relatively calm sea conditions during the cruise PS83. We plan to revisit this point in the future, when observations from more cruises are available.

For shipborne operation, the instrument's two-axis internal accelerometer is not sufficient to determine its position and alignment. While highly accurate systems such as *Polarstern*'s navigation system measure the ship motion on most research vessels, an offset between the instrument and the ship's sensors due to an imperfect alignment can introduce additional uncertainty. Hence, an upgrade of the instrument with a sensor capable of measuring its position also in dynamically moving environments would further improve its usability for shipborne operation.

The accuracy of the calculation of the direct irradiance from the sweep data using extrapolation to estimate the blocked diffuse irradiance by the shadowband (see Sect. 3.2) is still an open question. The extrapolation is done with a linear regression in the current processing algorithm and the uncertainty is assumed to be about 1 % for data measured when the sun is higher than 30° elevation. Since the blocked diffuse irradiance contains the aureole of the sun the uncertainty of this linear regression depends on the shape of the circum solar radiation, which in turn depends on aerosol type (Grassl, 1971). Therefore we expect the uncertainty to be higher for strongly forward scattering aerosol like desert dust, especially because we are using a broad shadowband, which occults up to 15° of the sky. Also, the occulting time of the sensor changes slightly with relative azimuth position of the sun to the radiometer. This may also affect the extrapolation of the blocked diffuse irradiance. In the future we will investigate the uncertainty of the estimated blocked diffuse irradiance in more detail, especially determining the effect of different aerosol types and azimuth dependence.

The calculation of the AOD from the direct beam transmittance is affected by an uncertainty of less than 0.02 for
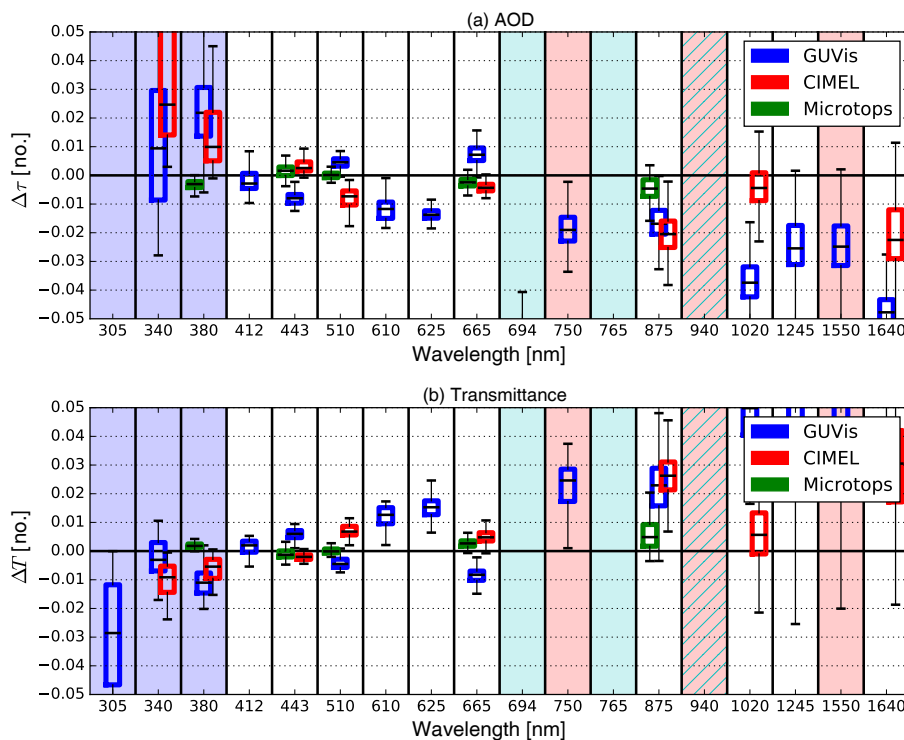
Figure 12. The panels show **(a)** AOD and **(b)** transmittance observations compared to values calculated with Eq. (25), which are expressed as difference of calculated and observed value. The Ångström exponent and curvature term are derived from a least-squared fit of the instrument AOD with 500 nm as the basis wavelength. The observations took place during the Melpitz Column experiment from May to July 2015 for the Cimel and GUVis instruments and at PS83 for the Microtops instrument. The channels are color-coded for known calibration or correction issues. Blue indicates issues with the radiation inlet, red channels rely on soft-coated filters, and channels marked with cyan are not corrected for gas absorption of H_2O and O_2. The data are displayed in a box and whisker plot. Shown are the median, boxes extending to the 25th percentile, and whiskers extending to the 75th percentile of the data.

all channels. This accuracy is comparable to Microtops sunphotometers (Ichoku, 2002), and close to a Cimel sunphotometer accuracy (Eck et al., 1999). The AOD calculation of AERONET and GUVis match closely as presented in Fig. 7, with minor differences caused by the different treatments of ozone and NO_2 absorption. Also, the direct comparison of the AOD retrieval with adjusted wavelengths shows only small deviations in lower wavelength channels due to different methods of deriving τ_{O_3} and τ_{NO_2}. As expected, sun photometry is more accurate on a land site.

Our uncertainty estimate and the comparison with sunphotometer observation presented here demonstrate that the GUVis shadowband radiometer is a reliable instrument for the observation of spectral irradiance components and aerosol properties both on land and on ships. For the latter, the automatic nature of its observations is a clear advantage over the Microtops instrument employed by MAN, which requires a human operator. The time series from the GUVis instrument is thus more continuous and has a higher time resolution than the time series of the Microtops. Nevertheless, one should be aware that in contrast to a human operator, the GUVis is mounted in a stationary position and thus cannot avoid

shadows from the ship super structure or the smoke plume. Hence, careful data analysis and quality screening of the raw data is essential to ensure high accuracy.

7   Conclusions and outlook

The 19-channel shadowband radiometer GUVis was operated for the first time on the research vessel *Polarstern* during its cruise PS83, with the aim of providing automated measurements on the radiative effects and optical properties of aerosol as part of the OCEANET project (Macke, 2009). Due to its continuously moving shadowband, this instrument allows to determine the direct, diffuse and global components of the solar irradiance on a moving platform with high accuracy.

In this paper, the data analysis implemented at TROPOS is described, including algorithms for cloud masking, motion and cosine error correction, the separation of the different irradiance components and the calculation of direct sun products. These methods are based to a large extent on Morrow et al. (2010) and Alexandrov et al. (2002) and have been adapted for application to the GUVis instrument. The

calculation of spectral AOD accounts for contributions by Rayleigh scattering and gas absorption to the total atmospheric optical depth and uses satellite products for obtaining the column concentrations of O_3 and NO_2.

Our results confirm that the GUVis instrument can provide automated and accurate measurements of the spectral irradiance components and the optical properties of aerosol on ships. Especially the observation of all three spectral radiation components simultaneously with one sensor is an advantage in comparison to sunphotometers, which only measure the direct component. Due to its stationary position, however, the influence of the ship exhaust needs to be taken into account. More observations are also required to assess the long time stability and the uncertainty under high-swell conditions.

Some questions still remain concerning filter stability, calibration accuracy, the accuracy of the extrapolated diffuse irradiance from the sweep data and the overall retrieval performance, which we plan to investigate in future work. In the next years, the GUVis instrument will be routinely operated as part of the TROPOS OCEANET container on RV *Polarstern* to carry out measurements of spectral irradiances and AOD and to investigate the solar radiation budget over the Atlantic Ocean. Regular calibrations of the instrument are planned to ensure the stability and overall performance of the instrument. Here, cross calibration with a AERONET Cimel sunphotometer on land constitutes an accurate alternative to laboratory calibrations, but only for the channels also available from the AERONET instruments.

For the calibration strategy of the GUVis in the future, it is planned to carry out an extensive Langley calibration on an high-altitude site as a base calibration. This is also mandatory to provide more confidence in the reliability of all spectral channels. Further laboratory calibrations will be consistently repeated to determine the drift of the spectral filters. Together with the Langley calibration, this will decrease the calibration uncertainty from the current 2 to about 1 % (Schmid and Wehrli, 1995). When possible during land-side measurement campaigns we going to apply a cross calibration to a AERONET Cimel sunphotometer to monitor temporal changes in the calibration (Ichoku, 2002).

Besides the current set of products, we are planning to implement further aerosol products such as the single scattering albedo and asymmetry parameter by using the diffuse to direct ratio as outlined by Herman et al. (1975) and applied in a number of aerosol studies (e.g., Petters et al., 2003; Kassianov et al., 2007). The GUVis is very well suited for this use because the diffuse and direct irradiance are measured simultaneously with only one sensor, causing negligible cross-calibration uncertainty.

A synergistic analysis also utilizing images from the all sky camera will allow an improved detection of clouds (Heinle et al., 2010). Specifically, this can help to improve the identification of short periods with cloud gaps, thereby enhancing the interpretation in broken cloud conditions and

improving the separation of cloud and aerosol radiative effects. Targeting clouds, an adaptation of the retrieval methods presented by Brückner et al. (2014) and Min and Harrison (1996), could be applied to estimate cloud properties from the GUVis measurements either stand-alone or in synergy with microwave radiometer observations. Finally, supersite observations including active instruments such as cloud radar and lidar could be used to extend previous efforts directed at testing radiation closure studies (e.g., Ebell et al., 2011) to narrowband irradiance observations.

8 Data availability

Supplementary data are available at Witthuhn et al. (2017).

References

Alexandrov, M. D., Lacis, A. A., Carlson, B. E., and Cairns, B.: Remote Sensing of Atmospheric Aerosols and Trace Gases by Means of Multifilter Rotating Shadowband Radiometer, Part I: Retrieval Algorithm, J. Atmos. Sci., 59, 524–543, doi:10.1175/1520-0469(2002)059<0524:RSOAAA>2.0.CO;2, 2002.

Alexandrov, M. D., Kiedron, P., Michalsky, J. J., Hodges, G., Flynn, C. J., and Lacis, A. A.: Optical depth measurements by shadowband radiometers and their uncertainties, Appl. Opt., 46, 8027, doi:10.1364/AO.46.008027, 2007.

Alexandrov, M. D., Lacis, A. A., Carlson, B. E., and Cairns, B.: Characterization of atmospheric aerosols using MFRSR measurements, J. Geophys. Res., 113, D08204, doi:10.1029/2007JD009388, 2008.

Bannehr, L. and Schwiesow, R.: A Technique to Account for the Misalignment of Pyranometers Installed on Aircraft, J. Atmos. Ocean. Tech., 10, 774–777, doi:10.1175/1520-0426(1993)010<0774:ATTAFT>2.0.CO;2, 1993.

Bartholomew, M. J., Reynolds, R. M., Vogelmann, A. M., Min, Q., Edwards, R., and Smith, S.: Design of a Shadowband Spectral Radiometer for the Retrieval of Thin Cloud Optical Depth, Liquid Water Path, and the Effective Radius, J. Atmos. Ocean. Tech., 28, 1458–1465, doi:10.1175/JTECH-D-11-00039.1, 2011.

Beer, A.: Bestimmung der Absorption des rothen Lichts in farbigen Fluessigkeiten, Annalen der Physik und Chemie, 86, 78–88, 1852.

Bhartia, P. K.: OMI Algorithm Theortical Basis Document, Tech. Rep. Vol II, NASA GSFC, available at: http://eospso.nasa.gov/sites/default/files/atbd/ATBD-OMI-02.pdf (last access: 14 December 2016), 2002.

Bodhaine, B. A., Wood, N. B., Dutton, E. G., and Slusser, J. R.: On Rayleigh Optical Depth Calculations, J. Atmos. Ocean. Tech., 16, 1854–1861, doi:10.1175/1520-0426(1999)016<1854:orodc>2.0.co;2, 1999.

Boers, R., Mitchell, R. M., and Krummel, P. B.: Correction of aircraft pyranometer measurements for diffuse radiance and alignment errors, J. Geophys. Res., 103, 16753, doi:10.1029/98JD01431, 1998.

Boucher, O., Randall, D., Artaxo, P., Bretherton, C., Feingold, G., Forster, P., Kerminen, V.-M., Kondo, Y., Liao, H., Lohmann, U., Rasch, P., Satheesh, S., Sherwood, S., Stevens, B., and Zhang, X.: Clouds and Aerosols, Cambridge University Press, Cambridge, United Kingdom and New York, NY, USA, 7, 571–658, doi:10.1017/CBO9781107415324.016, 2013.

Brückner, M., Pospichal, B., Macke, A., and Wendisch, M.: A new multispectral cloud retrieval method for ship-based solar transmissivity measurements, J. Geophys. Res.-Atmos., 119, 11338–11354, doi:10.1002/2014jd021775, 2014.

Bucsela, E. J., Krotkov, N. A., Celarier, E. A., Lamsal, L. N., Swartz, W. H., Bhartia, P. K., Boersma, K. F., Veefkind, J. P., Gleason, J. F., and Pickering, K. E.: A new stratospheric and tropospheric NO_2 retrieval algorithm for nadir-viewing satellite instruments: applications to OMI, Atmos. Meas. Tech., 6, 2607–2626, doi:10.5194/amt-6-2607-2013, 2013.

Chance, K.: OMI Algorithm Theortical Basis Document, Tech. Rep. Vol IV, Smithsonian Astrophysical Observatory, available at: http://eospso.nasa.gov/sites/default/files/atbd/ATBD-OMI-04.pdf (last access: 14 December 2016), 2002.

Ebell, K., Crewell, S., Löhnert, U., Turner, D. D., and O'Connor, E. J.: Cloud statistics and cloud radiative effect for a low-mountain site, Q. J. Roy. Meteorol. Soc., 137, 306–324, doi:10.1002/qj.748, 2011.

Eck, T. F., Holben, B. N., Reid, J. S., Dubovik, O., Smirnov, A., O'Neill, N. T., Slutsker, I., and Kinne, S.: Wavelength dependence of the optical depth of biomass burning, urban, and desert dust aerosols, J. Geophys. Res.-Atmos., 104, 31333–31349, doi:10.1029/1999jd900923, 1999.

Grassl, H.: Calculated Circumsolar Radiation as a Function of Aerosol Type, Field of View, Wavelength, and Optical Depth, Appl. Opt., 10, 2542, doi:10.1364/ao.10.002542, 1971.

Gueymard, C. A.: The sun's total and spectral irradiance for solar energy applications and solar radiation models, Sol. Energy, 76, 423–453, doi:10.1016/j.solener.2003.08.039, 2004.

Halthore, R. N., Eck, T. F., Holben, B. N., and Markham, B. L.: Sun photometric measurements of atmospheric water vapor column abundance in the 940 nm band, J. Geophys. Res., 102, 4343–4352, doi:10.1029/96jd03247, 1997.

Harrison, L., Michalsky, J., and Berndt, J.: Automated multifilter rotating shadow-band radiometer: an instrument for optical depth and radiation measurements, Appl. Opt., 33, 5118, doi:10.1364/ao.33.005118, 1994.

Haywood, J. M., Ramaswamy, V., and Soden, B. J.: Tropospheric Aerosol Climate Forcing in Clear-Sky Satellite Observations over the Oceans, Science, 283, 1299–1303, doi:10.1126/science.283.5406.1299, 1999.

Heinle, A., Macke, A., and Srivastav, A.: Automatic cloud classification of whole sky images, Atmos. Meas. Tech., 3, 557–567, doi:10.5194/amt-3-557-2010, 2010.

Herman, B. M., Browning, R. S., and Luisi, J. J. D.: Determination of the Effective Imaginary Term of the Complex Refractive Index of Atmospheric Dust by Remote Sensing: The Diffuse-Direct Radiation Method, J. Atmos. Sci., 32, 918–925, doi:10.1175/1520-0469(1975)032<0918:DOTEIT>2.0.CO;2, 1975.

Hodges, G. and Michalsky, J.: Multifilter Rotating Shadowband Radiometer (MFRSR) Handbook, WMO, doi:10.2172/1020261, 2011.

Holben, B., Eck, T., Slutsker, I., Tanre, D., Buis, J., Setzer, A., Vermote, E., Reagan, J., Kaufman, Y., Nakajima, T., Lavenu, F., Jankowiak, I., and Smirnov, A.: AERONET – A Federated Instrument Network and Data Archive for Aerosol Characterization, Remote Sens. Environ., 66, PII S0034-4257(98)00031-5, doi:10.1016/S0034-4257(98)00031-5, 1998.

Hooker, S. B., Bernhard, G., Morrow, J. H., Booth, C. R., Comer, T., Lind, R. N., and Quang, V.: Optical Sensors for Planetary Radiant Energy (OSPREy): calibration and Validation of Current and Next-Generation NASA Missions., NASA Goddard Space Flight Center, NASA/TM–2011–215872, http://ntrs.nasa.gov/search.jsp?R=20130003503 (last access: 10 February 2016), 2012.

Ichoku, C.: Analysis of the performance characteristics of the five-channel Microtops II Sun photometer for measuring aerosol optical thickness and precipitable water vapor, J. Geophys. Res., 107, AAC 5-1–AAC 5-17, doi:10.1029/2001jd001302, 2002.

Witthuhn, J., Deneke, H., Macke, A., and Bernhard, G.: Shipborne rotating shadowband radiometer data of spectral irradiance components and aerosol optical depth during POLARSTERN cruise PS83 (ANT-XXIX/10), doi:10.1594/PANGAEA.872377, 2017.

Kassianov, E. I., Flynn, C. J., Ackerman, T. P., and Barnard, J. C.: Aerosol single-scattering albedo and asymmetry parameter from MFRSR observations during the ARM Aerosol IOP 2003, Atmos. Chem. Phys., 7, 3341–3351, doi:10.5194/acp-7-3341-2007, 2007.

Kasten, F.: A new table and approximation formula for the relative optical airmass, Arch. Meteor. Geophy. B, 14, 206–223, doi:10.1007/bf02248840, 1965.

Kaufman, Y. J.: Aerosol optical thickness and atmospheric path radiance, J. Geophys. Res., 98, 2677, doi:10.1029/92jd02427, 1993.

King, D. and Myers, D.: Silicon-photodiode pyranometers: operational characteristics, historical experiences, and new calibration procedures, Conference Record of the Twenty Sixth IEEE Photovoltaic Specialists Conference, doi:10.1109/pvsc.1997.654323, 1997.

King, M. D. and Byrne, D. M.: A Method for Inferring Total Ozone Content from the Spectral Variation of Total Optical Depth Obtained with a Solar Radiometer, J. Atmos. Sci., 33, 2242–2251, doi:10.1175/1520-0469(1976)033<2242:amfito>2.0.co;2, 1976.

King, M. D., Byrne, D. M., Herman, B. M., and Reagan, J. A.: Aerosol Size Distributions Obtained by Inversions of Spectral Optical Depth Measurements, J. Atmos. Sci., 35, 2153–2167, doi:10.1175/1520-0469(1978)035<2153:asdobi>2.0.co;2, 1978.

Macke, A. (Ed.): The expedition of the research vessel "Polarstern" to the Antarctic in 2008 (ANT-XXIV/4), Berichte zur Polar- und

Meeresforschung (Reports on Polar and Marine Research), Alfred Wegener Institute for Polar and Marine Research, Bremerhaven, 591, 64 pp., hdl:10013/epic.32648.d001, 2009.

Mayer, B. and Kylling, A.: Technical note: The libRadtran software package for radiative transfer calculations – description and examples of use, Atmos. Chem. Phys., 5, 1855–1877, doi:10.5194/acp-5-1855-2005, 2005.

McPeters, R., Kroon, M., Labow, G., Brinksma, E., Balis, D., Petropavlovskikh, I., Veefkind, J. P., Bhartia, P. K., and Levelt, P. F.: Validation of the Aura Ozone Monitoring Instrument total column ozone product, J. Geophys. Res., 113, D15S14, doi:10.1029/2007jd008802, 2008.

Michalsky, J. J., Liljegren, J. C., and Harrison, L. C.: A comparison of Sun photometer derivations of total column water vapor and ozone to standard measures of same at the Southern Great Plains Atmospheric Radiation Measurement site, J. Geophys. Res., 100, 25995, doi:10.1029/95jd02706, 1995.

Miller, M. A., Bartholomew, M. J., and Reynolds, R. M.: The Accuracy of Marine Shadow-Band Sun Photometer Measurements of Aerosol Optical Thickness and Ångström Exponent, J. Atmos. Ocean. Tech., 21, 397–410, doi:10.1175/1520-0426(2004)021<0397:taomss>2.0.co;2, 2004.

Min, Q. and Duan, M.: Simultaneously retrieving cloud optical depth and effective radius for optically thin clouds, J. Geophys. Res., 110, D21201, doi:10.1029/2005JD006136, 2005.

Min, Q. and Harrison, L. C.: Cloud properties derived from surface MFRSR measurements and comparison with GOES results at the ARM SGP Site, Geophys. Res. Lett., 23, 1641–1644, doi:10.1029/96gl01488, 1996.

Morrow, J. H., Hooker, S. B., Booth, C. R., Bernhard, G., Lind, R. N., and Brown, J. W.: Advances in measuring the apparent optical properties (AOPs) of optically complex waters, National Aeronautics and Space Administration, Goddard Space Flight Center, 2010.

Pérez-Ramírez, D., Whiteman, D. N., Smirnov, A., Lyamani, H., Holben, B. N., Pinker, R., Andrade, M., and Alados-Arboledas, L.: Evaluation of AERONET precipitable water vapor versus microwave radiometry, GPS, and radiosondes at ARM sites, J. Geophys. Res.-Atmos., 119, 9596–9613, doi:10.1002/2014jd021730, 2014.

Petters, J. L., Saxena, V. K., Slusser, J. R., Wenny, B. N., and Madronich, S.: Aerosol single scattering albedo retrieved from measurements of surface UV irradiance and a radiative transfer model, J. Geophys. Res., 108, D94288, doi:10.1029/2002jd002360, 2003.

Reynolds, R. M., Miller, M. A., and Bartholomew, M. J.: Design, Operation, and Calibration of a Shipboard Fast-Rotating Shadowband Spectral Radiometer, J. Atmos. Ocean. Tech., 18, 200–214, doi:10.1175/1520-0426(2001)018<0200:DOACOA>2.0.CO;2, 2001.

Schmid, B. and Wehrli, C.: Comparison of Sun photometer calibration by use of the Langley technique and the standard lamp, Appl. Opt., 34, 4500, doi:10.1364/ao.34.004500, 1995.

Schmid, B., Thorne, K. J., Demoulin, P., Peter, R., Maetzler, C., and Sekler, J.: Comparison of modeled and empirical approaches for retrieving columnar water vapor from solar transmittance measurements in the 0.94 µm region, J. Geophys. Res., 101, 9345, doi:10.1029/96jd00337, 1996.

Schneider, W., Moortgat, G. K., Tyndall, G. S., and Burrows, J. P.: Absorption cross-sections of NO_2 in the UV and visible region (200–700 nm) at 298 K, J. Photoch. Photobio. A, 40, 195–217, doi:10.1016/1010-6030(87)85001-3, 1987.

Seckmeyer, G. and Bernhard, G.: Cosine error correction of spectral UV-irradiances, P. Soc. Photo.-Opt. Ins., doi:10.1117/12.163505, 1993.

Seckmeyer, G., Bais, A., Bernhard, G., Blumthaler, M., Johnsen, B., Lantz, K., and McKenzie, R.: Instruments to Measure Solar Ultraviolet Radiation – Part 3: Multi-channel filter instruments, Global Atmosphere Watch Report, World Meteorological Organization, Geneva, Switzerland, https://www.wmo.int/pages/prog/arep/gaw/documents/GAW190_TD_No_1537_web.pdf (last access: 10 February 2016), 2010.

Serdyuchenko, A., Gorshelev, V., Weber, M., Chehade, W., and Burrows, J. P.: High spectral resolution ozone absorption cross-sections – Part 2: Temperature dependence, Atmos. Meas. Tech., 7, 625–636, doi:10.5194/amt-7-625-2014, 2014.

Shettle, E. P.: Models of aerosols, clouds, and precipitation for atmospheric propagation studies, in: AGARD, Atmospheric Propagation in the UV, Visible, IR, and MM-Wave Region and Related Systems Aspects 14 p (SEE N90-21907 15-32), 454 pp., http://adsabs.harvard.edu/abs/1990apuv.agar.....S (last access: 13 October 2016), 1990.

Smirnov, A., Holben, B., Eck, T., Dubovik, O., and Slutsker, I.: Cloud-Screening and Quality Control Algorithms for the AERONET Database, Remote Sens. Environ., 73, 337–349, doi:10.1016/s0034-4257(00)00109-7, 2000.

Smirnov, A., Holben, B. N., Kaufman, Y. J., Dubovik, O., Eck, T. F., Slutsker, I., Pietras, C., and Halthore, R. N.: Optical Properties of Atmospheric Aerosol in Maritime Environments, J. Atmos. Sci., 59, 501–523, doi:10.1175/1520-0469(2002)059<0501:opoaai>2.0.co;2, 2002.

Smirnov, A., Holben, B. N., Lyapustin A., Slutsker, I., and Eck, T. F.: AERONET processing algorithms refinement, AERONET Workshop, El Arenosillo, Spain, 2004.

Smirnov, A., Holben, B. N., Slutsker, I., Giles, D. M., McClain, C. R., Eck, T. F., Sakerin, S. M., Macke, A., Croot, P., Zibordi, G., Quinn, P. K., Sciare, J., Kinne, S., Harvey, M., Smyth, T. J., Piketh, S., Zielinski, T., Proshutinsky, A., Goes, J. I., Nelson, N. B., Larouche, P., Radionov, V. F., Goloub, P., Krishna Moorthy, K., Matarrese, R., Robertson, E. J., and Jourdin, F.: Maritime Aerosol Network as a component of Aerosol Robotic Network, J. Geophys. Res.-Atmos., 114, D06204, doi:10.1029/2008JD011257, 2009.

Toledano, C., Cachorro, V. E., Berjon, A., de Frutos, A. M., Sorribas, M., de la Morena, B. A., and Goloub, P.: Aerosol optical depth and Ångström exponent climatology at El Arenosillo AERONET site (Huelva, Spain), Q. J. Roy. Meteorol. Soc., 133, 795–807, doi:10.1002/qj.54, 2007.

WMO: Guide to meteorological instruments and methods of observation, World Meteorological Organization Bulletin, 8, Chapter 7: "Measurements of Radiation" – ANNEX 7.D, www.wmo.int/pages/prog/www/IMOP/CIMO-Guide.html (last access: 2 March 2017), 2010.